

An assessment of Landsat-8 atmospheric correction schemes and remote sensing reflectance products in coral reefs and coastal turbid waters



Jianwei Wei^{a,*}, Zhongping Lee^a, Rodrigo Garcia^a, Laura Zoffoli^a, Roy A. Armstrong^b, Zhehai Shang^a, Patrick Sheldon^a, Robert F. Chen^a

^a School for the Environment, University of Massachusetts Boston, Boston, MA, USA

^b Department of Marine Sciences, University of Puerto Rico, Mayagüez, PR, USA

ARTICLE INFO

Keywords:

Landsat-8
Atmospheric correction
Remote sensing reflectance
Coral reefs
Ocean color

ABSTRACT

The Operational Land Imager (OLI) onboard Landsat-8 satellite can provide remote sensing reflectance (R_{rs}) of aquatic environments with high spatial resolution (30 m), allowing for benthic habitat mapping and monitoring of bathymetry and water column optical properties. To facilitate these applications, accurate sensor-derived R_{rs} is required. In this study, we assess atmospheric correction schemes, including NASA's NIR-SWIR approach, Acolite's NIR and SWIR approaches and the cloud-shadow approach. We provide the first comprehensive evaluation for Landsat-8 R_{rs} retrievals in optically shallow coral reefs, along with an investigation of Landsat-8 R_{rs} products in a temperate turbid embayment. The obtained Landsat-8 R_{rs} data products are evaluated with concurrent *in situ* hyperspectral R_{rs} measurements. Our analyses show that the NASA and the cloud-shadow approaches generated reliable R_{rs} products across shallow coral reefs and optically deep waters. This evaluation suggests that high quality R_{rs} products are achievable from the Landsat-8 satellite in optically shallow environments, which supports further application of Landsat-8 type measurements for coral reef studies.

1. Introduction

Aquatic biodiversity and environmental science have entered a new era with the availability of advanced ocean color remote sensing imagers (Turner et al., 2015). Among many other remote sensors, such as those operated by NASA, NOAA, USGS and ESA, Landsat-8 satellite is the continuation mission to its predecessors with coverage of coastal ecosystems (Loveland and Irons, 2016; Roy et al., 2014). The Operational Land Imager (OLI) onboard Landsat-8 can provide remote sensing reflectance (R_{rs} , sr^{-1}) of aquatic environments with high spatial resolution (30 m), allowing the monitoring of aquatic ecology and associated environmental parameters (e.g., Andréfouët et al., 2001; Olmanson et al., 2008; Palandro et al., 2008). Currently, quantitative evaluation of Landsat-8 R_{rs} products in optically diverse aquatic environments, particularly of shallow waters including coral reefs, is rare. Non-validated Landsat-8 R_{rs} products limit their applicability and introduce unknown uncertainties in aquatic ecology and water quality studies in coastal environments.

The OLI instrument is equipped with four visible bands (443, 482, 561 and 655 nm) and has improved signal-to-noise ratios (SNR) (Schott et al., 2016) and radiometric calibration (Markham et al., 2014). Thus it has the potential to retrieve R_{rs} products with a higher quality

compared to its predecessors. Retrieval of R_{rs} products from ocean color satellites requires an atmospheric correction (AC) algorithm (IOCCG, 2010). Existing operational AC schemes were primarily developed for clear oceanic waters (Gordon and Wang, 1994), where the assumption of zero water-leaving radiance (L_w , $\mu\text{W cm}^{-2} \text{sr}^{-1} \text{nm}^{-1}$) at the near-infrared (NIR) bands is valid (a.k.a. "black pixels"). For more turbid waters, a combination of NIR and shortwave-infrared (SWIR) bands are used to select the aerosol types (Wang and Shi, 2007), with any non-negligible L_w derived with an iterative approach (Bailey et al., 2010) through NASA's SeaDAS processing software (Franz et al., 2015). Acolite is another radiative transfer (RT)-based AC system (Vanhellemont and Ruddick, 2014, 2015). Both SeaDAS and Acolite systems can be used for atmospheric correction of Landsat-8 Level-1 measurements. In addition, some *ad hoc* AC approaches have been developed and applied that utilize radiative transfer-based codes such as 6S model (Giardino et al., 2014). Further, image-based models have also shown promise to aid atmospheric correction for both optically shallow and deep environments (Amin et al., 2014; Lee et al., 2007; Zhang et al., 2017). Despite the wide spectrum of available AC schemes, the performance of these algorithms in optically shallow waters is rarely evaluated. It remains uncertain which AC scheme can deliver reliable R_{rs} products from Landsat-8 measurements in various water bodies.

* Corresponding author.

E-mail address: jianwei.wei@umb.edu (J. Wei).

The R_{rs} products of operational ocean color satellites (e.g., MODIS Aqua and SNPP VIIRS) are usually validated through dedicated efforts with the use of radiometrically and spectrally accurate *in situ* R_{rs} matchups retrieved within a short period of time from an overpass (± 3 h) (Hlaing et al., 2014; Mélin et al., 2007; Zibordi et al., 2009b). However, the lack of *in situ* matchup data hinders the validation of the Landsat-8 R_{rs} products. Among the earlier efforts, Zheng et al. (2016) presented a dozen *in situ* and Landsat-8 R_{rs} matchups in an extremely turbid lake but with the matchup time relaxed to ± 6 h; a large time window might contribute significantly to the differences observed between field and satellite data. Pahlevan et al. (2016) provided some preliminary results of Landsat-8 R_{rs} data in Boston Harbor but focused on the Acolite scheme. With the Ocean Color Aerosol Robotic Network (AERONET-OC) (Zibordi et al., 2006) data, Pahlevan et al. (2017) further evaluated the performance of the AC schemes implemented in SeaDAS and reported that a combination of the 865 nm and 2201 nm bands provided generally better R_{rs} products. Although the Landsat-8 products can be “cross-validated” with other available ocean color satellite products (Qiu et al., 2017), the data quality of the reference data used therein is often underdetermined. To date, Landsat-8 R_{rs} products are rarely evaluated in optically shallow environments, despite the important value of Landsat-8 imagery in shallow water remote sensing (Lymburner et al., 2016; Pacheco et al., 2015). The earlier qualitative assessments of Landsat-8 R_{rs} retrievals were limited by available matchup data (Giardino et al., 2014; Yadav et al., 2017). Considering these existing issues and challenges with data product validations, it is critical that the performance of Landsat-8 be thoroughly assessed with accurate *in situ* matchups for a wide range of nearshore waters.

Our objective is to quantitatively assess the performance of existing AC schemes for Landsat-8 in coral reefs and turbid water environments that include NASA's standard NIR-SWIR approach (Franz et al., 2015), the Acolite approach (Vanhellemont and Ruddick, 2014, 2015), and the cloud-shadow approach (CSA) (Lee et al., 2007). To our best knowledge, this is the first comprehensive evaluation of Landsat-8 R_{rs} retrievals in optically shallow coral reef waters. All R_{rs} retrievals are validated with concurrent high-quality *in situ* measurements of hyperspectral R_{rs} spectra (within ± 1.5 h of overpass). We demonstrate that the NASA and the cloud-shadow approaches generate the most reliable R_{rs} retrievals across shallow coral reefs and optically deep waters. It is confirmed that the Landsat-8 instrument can indeed provide high quality R_{rs} measurements for optically shallow waters.

2. Data and methods

2.1. Study areas

The *in situ* radiometric measurements for this effort were conducted in a broad range of aquatic environments. They include the optically shallow coral reef environments of La Parguera Natural Reserve, Puerto Rico (Fig. 1A), Maui, Hawaii (Fig. 1B), and Florida Keys (Fig. 1C). The La Parguera Natural Reserve has the most extensive coral reef ecosystem in Puerto Rico as well as a coastal mangrove fringe, mangrove islands and seagrass meadows (Pittman et al., 2010). The patch reefs consist mostly of hard and soft corals (Fig. 2A), with abundant seagrasses on the shallow back-reef lagoons (Fig. 2B). The water depths vary from ~ 1 m up to 20–30 m at the shelf edge. The chlorophyll a concentrations (CHL, mg m^{-3}) at these sites are ~ 0.2 – 0.3 mg m^{-3} (Otero and Carbery, 2005). The southwest coasts of Maui have abundant fringe corals with diverse species, which are under great environmental pressures (Prouty et al., 2017; Rodgers et al., 2015). Our measurements in Maui were obtained from 15 sites distributed in Kakehihi, Launiupoko and Olowalu areas, where the natural coral formations provide a canopy of hard corals (Fig. 2C and Fig. 2D) that are structurally complex with water depths varying from ~ 1 m to 10 m. These Maui stations are characteristic of extremely clear waters, with CHL as low as $\sim 0.15 \text{ mg m}^{-3}$ (Wedding et al., 2018). Four stations

were measured in the coral reefs of Florida Keys with water depths ranging from 3 to 7 m, where the CHL varies around 0.3 – 0.6 mg m^{-3} .

The waters of Massachusetts Bay (Fig. 1D) are usually strongly stratified in summer and autumn, but various factors, including tides, winds, and buoyancy gradients affect water properties and their distributions. The chlorophyll a concentrations in these relatively turbid waters are on average $\sim 1.5 \text{ mg m}^{-3}$. Boston Harbor is a tide-dominated environment with contributions from several major rivers that include the Charles River, Mystic River and Neponset River. The waters have annual average concentrations of suspended particulate matter (SPM) varying from 3 to 8 mg l^{-1} and CHL from 2 to 5 mg m^{-3} (Taylor, 2016).

2.2. In situ hyperspectral remote sensing reflectance and data reduction

A total of 13 field trips were conducted between July 2013 and October 2017, coinciding with Landsat-8 satellite overpasses (Table 1). During each field campaign, a downward-looking hyperspectral ocean color radiometer (HyperOCR, Satlantic Inc.) attached with a skylight-blocking apparatus (SBA) was used to directly measure the water-leaving radiance, while an upward-looking hyperspectral radiometer (HyperOCR, Satlantic Inc.) was employed to measure the downwelling plane irradiance (E_d , $\mu\text{W cm}^{-2} \text{ nm}^{-1}$). The two radiometers were calibrated over the spectral domain between ~ 350 – 800 nm, with a spectral interval of 3 nm (FWHM 10 nm) and a radiometric calibration uncertainty of $< 2.5\%$ for radiance and 1.5% for irradiance (Voss et al., 2010). The SBA system measures L_w with small uncertainty (refer to Section 4.1) and high accuracy by blocking the light from the sky reflected off the water surface (Lee et al., 2013). In addition, a depth sounder was integrated to simultaneously measure water depths. A GPS sensor and an underwater high definition (HD) camera were also attached to provide coordinates (± 3 m precision) and images of bottom substrates, respectively.

To reduce the R_{rs} measurement uncertainty, the following protocol was adopted. First, the radiance and irradiance sensors were installed on two extended arms (30 cm long) so as to minimize the disturbance of the buoy (Fig. 2, Wei et al., 2015; <https://www.osapublishing.org/oe/abstract.cfm?uri=oe-23-9-11826>). The instrument package floated on the water's surface and simultaneously measured both E_d and L_w and depth for a period of 3–5 min. The instrument was also kept at a distance > 20 m from the small operation boat to avoid boat disturbance to the measurements. The raw data were calibrated to absolute radiometric units with the manufacturer's data processing software PROSOFT. The hyperspectral E_d measurements were then interpolated so that both E_d and L_w have exactly the same wavelengths. Both spectral E_d and L_w were further used to derive the instantaneous remote sensing reflectance (Wei et al., 2015), as

$$R_{rs}(\lambda, t) = \frac{L_w(\lambda, t)}{E_s(\lambda, t)} \quad (1)$$

with t for the observation time. The $R_{rs}(\lambda, t)$ data with instrument inclination $> 5^\circ$ were filtered out. To identify and filter-out potentially contaminated data points due to the radiometric system occasionally submerged in water or the SBA popped up in air, the following procedures were further developed and employed. First, the probability density function (PDF) of the $R_{rs}(\lambda, t)$ data sequence at a red band (usually 698 nm) was calculated with the Matlab® normal kernel smoothing function, ksdensity, at 100 equally spaced points that cover the range of the $R_{rs}(698, t)$ data. Then all $R_{rs}(\lambda, t)$ spectra with $R_{rs}(698, t)$ exceeding $\pm 15\%$ of its mode were removed. The mean $R_{rs}(\lambda)$ spectrum was then derived from the remaining $R_{rs}(\lambda, t)$ spectra. For measurements from Massachusetts Bay and Boston Harbor, the self-shading errors were corrected with the scheme specifically developed for the SBA system (Shang et al., 2017). No appropriate shade correction algorithm is available for shallow water measurements; nonetheless, the self-shading errors in coral reefs are small due to the strong contributions from bottom reflectance.

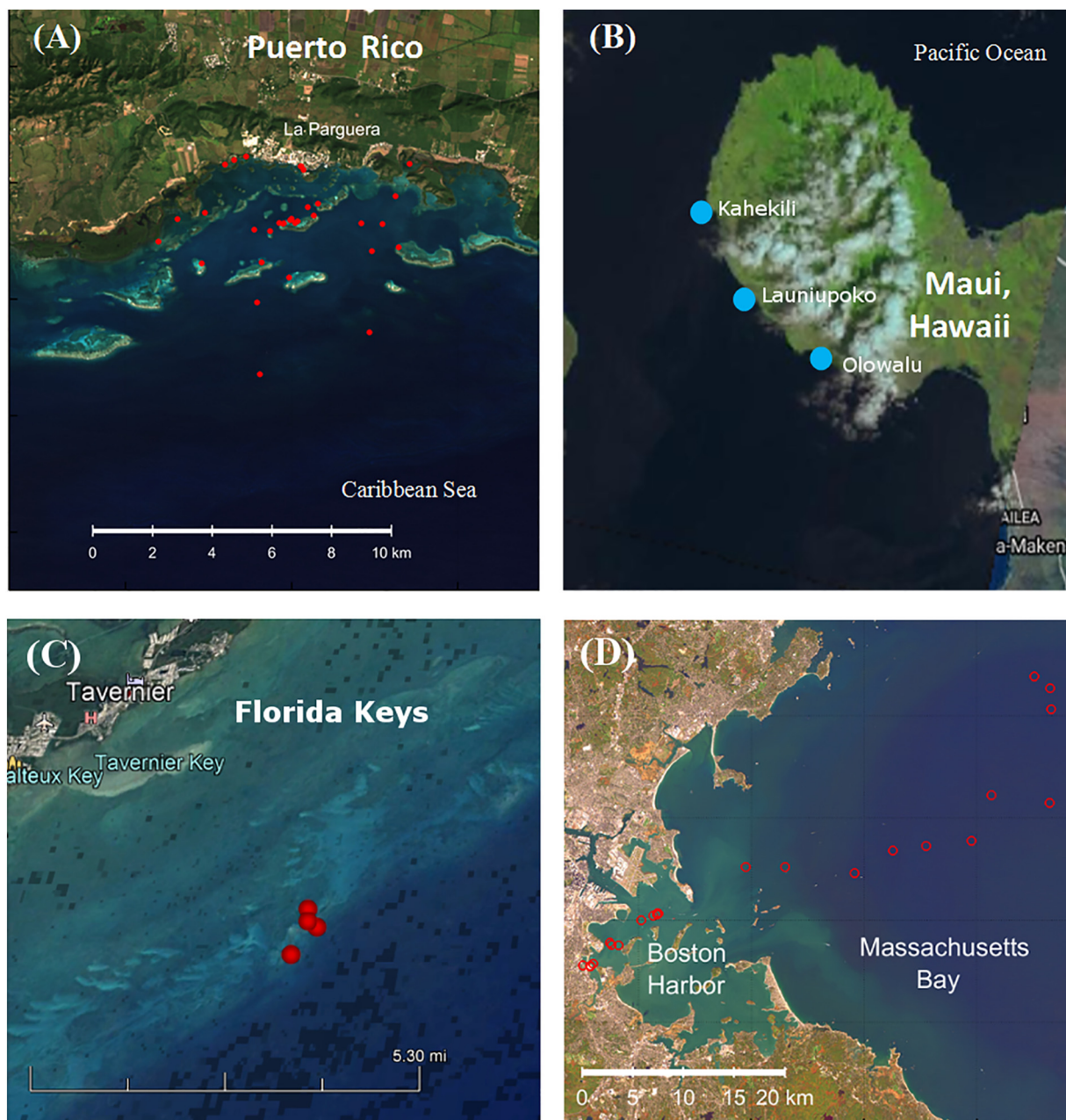


Fig. 1. (A) Discrete sampling stations of *in situ* optical measurements in the La Parguera Natural Reserve, Puerto Rico; (B) Sampling areas in the southwest coasts of Maui, Hawaii; (C) Discrete sampling stations in Florida Keys; (D) Discrete sampling stations in Boston Harbor and Massachusetts Bay. These true color images are derived from Landsat-8 data.

The Landsat-8 OLI imager has a wide bandpass of 15, 60, 57 and 37 nm for its four visible bands, respectively. To account for the bandpass mismatch, the *in situ* R_{rs} spectra were convolved with the OLI's relative spectral response (RSR) to generate the corresponding R_{rs} spectra at the four Landsat-8 bands:

$$R_{sr}(\lambda_0) = \frac{\int R_{sr}(\lambda) RSR(\lambda_0) d\lambda}{\int RSR(\lambda_0) d\lambda} \quad (2)$$

where λ_0 is used to represent an OLI band with a center wavelength of λ_0 . The full spectral RSR of OLI can be accessed online.

2.3. Atmospheric correction of Landsat-8 images

The Landsat-8 Level-1 data processed by the Level-1 Product Generation System (LPGS) were downloaded from the USGS

EarthExplorer gateway (<http://earthexplorer.usgs.gov>). A total of 7 bands at 443, 482, 561, 655, 865, 1609 and 2201 nm are included in this distribution. The OLI sensor quantizes data over a 12-bit dynamic range; the distributed products are, however, rescaled and delivered as 16-bit images (up to 55,000 Gy levels). The Landsat-8 images used for this study are described in Table 1.

The total radiance at Top of Atmosphere (TOA), L_t , is calibrated on-orbit and has been relatively stable (Markham et al., 2014). L_t can be decomposed into contributions of the atmosphere, water surface reflection and L_w according to:

$$L_t(\lambda) = L_{as}(\lambda) + T(\lambda)L_w(\lambda) \quad (3)$$

where L_{as} is the contribution from the atmosphere and sea surface reflectance, and T the transmittance of L_w from sea surface to sensor altitude. To retrieve L_w and then R_{rs} from the Level-1 products, two types

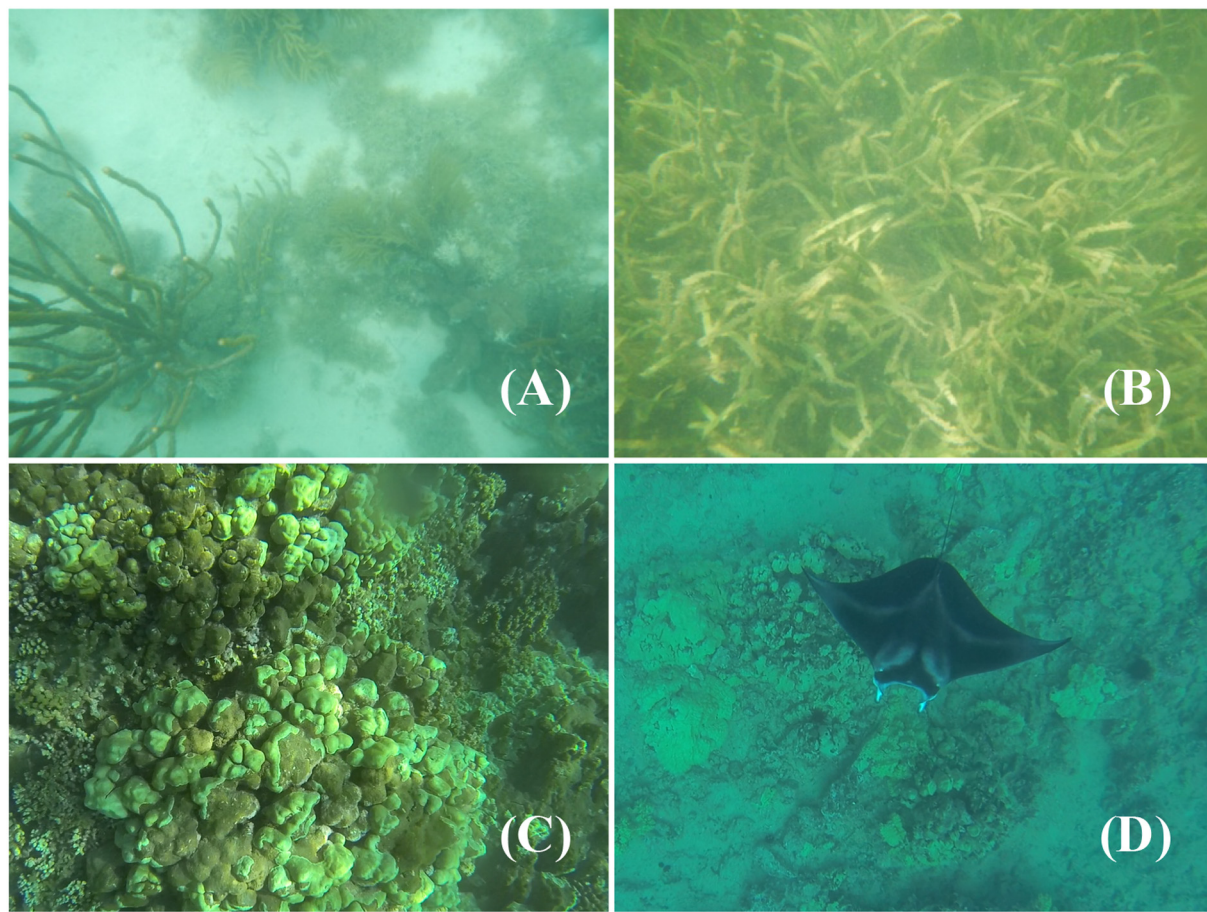


Fig. 2. (A) Patchy hard corals and soft corals and (B) seagrass in the La Parguera Natural Reserve; (C) hard coral beds (2 m bottom depth) and (D) hard corals (6 m bottom depth, with a manta ray captured in the view) in Maui.

Table 1

Landsat-8/OLI overpasses for comparison with *in situ* matchups. The symbols “ \times ” and “—” indicate the availability/unavailability of the R_{rs} products from the corresponding atmospheric corrections.

Study areas	Landsat-8 images	Acquisition time (UTC)	θ_s	Atmospheric correction			
				NASA standard	Acolite NIR/SWIR	Cloud Shadow	
Coral reefs	La Parguera, Puerto Rico	LC80050482013329	14:52	43°	\times	\times	
		LC80050482014124	14:50	23°	\times	\times	
		LO80050482015063 ^a	14:50	36°	—	\times	
		LC80050482015319	14:50	41°	\times	\times	
Turbid waters	Maui, Hawaii Florida Keys Massachusetts Bay and Boston Harbor	LC80640452017049	20:54	47°	\times	\times	
		LC80150432016088	15:50	32°	\times	\times	
		LC80110312013211	15:22	40°	\times	\times	
		LC80120312015240	15:26	38°	\times	\times	
		LC80120312015304	15:26	59°	\times	—	
		LC80120312016243	15:26	38°	\times	\times	
		LC80120312016259	15:26	44°	\times	\times	
		LC80120312017213 ^a	15:27	40°	—	—	
		LC80120312017277 ^a	15:27	61°	—	\times	

^a SeaDAS software (v7.4) is currently unable to process these images due to data compatibility problem.

of atmospheric correction schemes were adopted and assessed: radiative transfer-based systems (SeaDAS and Acolite) and an image-based approach (CSA), which are detailed in following texts.

NASA standard approach: The NASA atmospheric correction scheme was implemented by the SeaDAS data processing system (v7.4) (Franz et al., 2015). Specifically, a look-up table (LUT) of Rayleigh reflectance is pre-computed (Ahmad et al., 2010). The contributions of sunglint and whitecaps are modeled as a function of environmental conditions. Estimation of aerosol radiance is based on the updated aerosol models

which are further developed out of the AERONET observations (Ahmad et al., 2010). To relax the limitation of the “black pixel” assumption, an iterative scheme is used to estimate the aerosol radiance at the NIR and/or SWIR bands (Bailey et al., 2010). For Landsat-8 image processing, the OLI bands 5 and 7 (865 and 2201 nm, respectively) were chosen in the present study. This NIR-SWIR band combination yields the most robust R_{rs} in moderately turbid waters among all options implemented within SeaDAS (Pahlevan et al., 2017). All the estimations were conducted on a per-pixel basis. The residual glint correction was

performed with the standard approach (Wang and Bailey, 2001). The standard Level-2 quality flags including ATMFAIL (Atmospheric correction failure), LAND (land pixel), CLDICE (Probable cloud or ice contamination), and HILT (very high or saturated observed radiance) were masked. It is necessary to point out that because radiance is directionally dependent, L_w from Landsat-8 does not necessarily match the direction of L_w measured *in situ*, even when measurements were made at the same time. To reduce the impact of this angular mismatch in comparing the L_w (or R_{rs}) value from a satellite sensor with that from *in situ* measurement, it is necessary to employ a bidirectional reflectance distribution function (BRDF) in order to correct for this angular effect. The BRDF scheme of Morel et al. (2002) is included in SeaDAS, but is designed for oceanic Case-1 waters. In this effort, the BRDF correction was turned off because of the nature of either turbid coastal waters of Massachusetts Bay and Boston Harbor or the optically shallow waters of coral reefs. We acknowledge that not accounting for BRDF effect may add some extra uncertainty in the validation of the AC schemes considered in this study, but the impact of this factor is likely small compared to the other sources in an AC scheme (refer to Section 4.1).

On-orbit vicarious calibration of satellites is an important step for accurate retrieval of remote sensing reflectance (Bailey et al., 2008; Eplee et al., 2001). There is a set of calibration gains derived for Landsat-8 based on the SeaDAS system (Franz et al., 2015). But there are no gains developed specifically for the Acolite system. As a result, no vicarious calibration gains were applied in our analysis. But the uncertainty associated with vicarious calibration will be discussed later (refer to Section 4.1).

Acolite/NIR approach: The Acolite module (v20160520.1) uses NIR bands for aerosol determination (Vanhellemont and Ruddick, 2014), while a LUT generated from 6SV (Vermote et al., 2016) is used for the Rayleigh correction. The aerosol reflectance ratio ϵ in bands 4 and 5 (655 and 865 nm) can be derived from clear-water pixels where the water reflectance is negligible and thus where only the aerosols contribute to the TOA signal. A standard $\epsilon = 1$ is assumed to be constant over the whole image. Another assumption for the aerosol correction is made that the ratio of marine reflectance in these two bands, α , is constant (=8.7).

Acolite/SWIR approach: This option (v20160520.1) uses two SWIR bands (1609 and 2201 nm) for aerosol determination (Vanhellemont and Ruddick, 2015), where the marine signals are assumed negligible. Unlike the Acolite/NIR approach, the aerosol type ϵ is now determined on a per-pixel basis. In addition, a moving-average filter (kernel size = 32) is included to reduce the noise. Note that the Acolite scheme has no BRDF correction option to its R_{rs} products.

Cloud-shadow approach: The cloud-shadow approach is an image-based atmospheric correction scheme that is appropriate for high-

resolution imagery (Lee et al., 2007). It requires three radiance spectra to be determined from each image, including a bright pixel over clouds, a shadow pixel and an adjacent sunlit pixel. Specifically, we implemented this scheme with the following steps:

Step 1: The path radiance from the sea surface to the sensor, $L_{as}(\lambda)$, was estimated from a pair of adjacent sunlit pixel and shadow pixel (Lee et al., 2007)

$$L_{as}(\lambda) = L_t^{sun}(\lambda) - \frac{L_t^{sdw}(\lambda) - L_t^{sdw}(\lambda)}{1 - E_d^{sky}(\lambda)/E_d(\lambda)} \quad (4)$$

where L_t^{sdw} and L_t^{sun} are the radiance from a shadow pixel and adjacent sunlit pixel, respectively. The pair is close to each other to ensure that their environmental properties are identical. In our study, they are given in the units of digital counts. E_d^{sky} is the downwelling irradiance above the water surface from the diffuse skylight. Both E_d and E_d^{sky} were estimated from the RADTRAN model (Gregg and Carder, 1990) with knowledge of the solar zenith angles at the time of the Landsat-8 overpass. Note that the impact of errors of E_d^{sky}/E_d estimation on the results of L_{as} is small (Lee et al., 2007).

Step 2: The total radiance of clouds, $L_t^{cld}(\lambda)$, was extracted as the mean of the relatively brighter patch of clouds. It is cautioned that the cloud pixels selected should not make $L_t^{cld}(\lambda)$ saturated.

Step 3: With known $L_t^{cld}(\lambda)$ and derived $L_{as}(\lambda)$, the remote sensing reflectance for each pixel was determined:

$$R_{rs}(\lambda) = \rho \frac{L_t(\lambda) - L_{as}(\lambda)}{L_t^{cld}(\lambda) - L_{as}(\lambda)} \quad (5)$$

where $L_t(\lambda)$ is the total radiance obtained from the Landsat-8 Level-1 GeoTIFF images, and ρ is the cloud reflectance (units: sr^{-1}) corresponding to the cloud pixels selected.

The cloud reflectance is an image-dependent property and should be estimated independently. According to Eq. (5), ρ can be determined with known R_{rs} and L_t . Here, we assumed a spectrally flat cloud reflectance as in Lee et al. (2007). Then we used the following steps to determine ρ :

a) A deep-water pixel was located in a coincident SNPP VIIRS overpass using the Ocean Color Viewer (OCView) (Mikelsons and Wang, 2018). The time difference between VIIRS and Landsat-8 overpasses was about 2 h. The quality assurance (QA) scores (Wei et al., 2016) were accessible from the OCView, which objectively quantify the quality of individual VIIRS R_{rs} spectra with the scores varying from 0 to 1 (0 = lowest quality, 1 = highest quality). We only used R_{rs} spectra with QA scores > 0.8. In this study, the VIIRS remote sensing reflectance at 551 nm, $R_{rs}(551)$, varies from 0.0017 to 0.0019 sr^{-1} in the deep waters of Puerto Rico and Hawaii, and from 0.0021 to 0.0062 sr^{-1} in Massachusetts Bay and Boston Harbor, and is 0.0026 sr^{-1} in Florida Keys (see Table 2). It is further assumed that $R_{rs}(551)$ of VIIRS

Table 2
Optical properties used for the derivation of cloud reflectance for Landsat-8 images.

Study areas	Landsat-8 images	Landsat-8 radiance (units: digital counts)			$R_{rs}(551)$ (sr^{-1})	Lat & Lon (deg)	ρ (sr^{-1})
		$L_t(561)$	$L_{as}(561)$	$L_t^{cld}(561)$			
La Parguera, Puerto Rico	LC80050482013329	6740	6486	20,364	0.0019	17.7621, -67.3544	0.104
	LC80050482014124	8333	7394	24,281	0.0018	17.9654, -67.4849	0.032
	LC80050482015063	7371	6908	26,360	0.0017	17.7505, -67.0145	0.093
	LC80050482015319	6792	6599	26,658	0.0018	17.8802, -67.3943	0.187
Maui, Hawaii	LC80640452017049	6670	6404	25,945	0.0019	20.9070, -157.323	0.140
	LC80150432016088	7792	6800	22,994	0.0026	24.7343, -80.6781	0.042
Massachusetts Bay and Boston Harbor	LC80110312013211	7639	6949	16,460	0.0058	41.4761, -70.3606	0.080
	LC80120312015240	6903	6471	23,543	0.0015	42.3495, -70.4128	0.059
	LC80120312015304	–	–	–	–	–	–
	LC80120312016243	6774	6329	23,729	0.0022	42.3495, -70.3290	0.086
	LC80120312016259	6810	6449	19,325	0.0021	42.3592, -70.4100	0.075
	LC80120312017213	–	–	–	–	–	–
	LC80120312017277	6991	6195	19,530	0.0062	41.4803, -70.2837	0.104

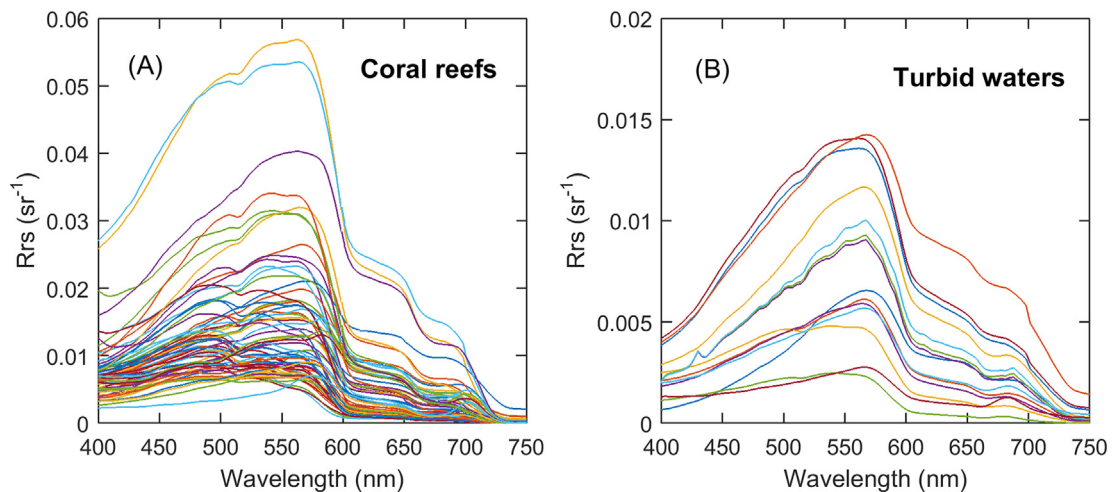


Fig. 3. Hyperspectral remote sensing reflectance spectra measured in (A) optically shallow coral reef environments and (B) optically deep waters of Massachusetts Bay and Boston Harbor.

approximates $R_{rs}(561)$ of Landsat-8.

b) The coordinates of the VIIRS pixel in Step a) were used to identify the corresponding Landsat-8 Level-1 pixel. The total radiance L_t (561) (units: digital counts) of this Landsat-8 pixel was then extracted. Assuming negligible difference in the remote sensing reflectance between the deep-water pixels of Landsat-8 (30 m) and VIIRS (750 m), we derived ρ from a variant form of Eq. (5) with the determined R_{rs} (551) and L_t (561), as below:

$$\rho = R_{rs}(551) \frac{L_t^{cld}(561) - L_{as}(561)}{L_t(561) - L_{as}(561)} \quad (6)$$

In this study it is found that the cloud reflectance varies between 0.032 and 0.187 sr^{-1} for the various clouds selected, with a mean value of $\sim 0.1 \text{ sr}^{-1}$ (Table 2).

There was no explicit sunglint correction employed for the images; and we only observed moderate sunglint in image LC80050482014124 from La Parguera, Puerto Rico.

2.4. In situ and satellite matchups and metrics

The satellite pixels with heavy cloud contamination were identified and discarded from subsequent analysis. Also, no *in situ* measurements within a short distance ($< 60 \text{ m}$) to shorelines were used. A time constraint of $\pm 1.5 \text{ h}$ was followed to create *in situ* and satellite matchups. It is noted that the satellite R_{rs} matchup spectra are often derived as the mean over a 3×3 pixel neighborhood, where the coefficient of variation of R_{rs} measurements is small (Bailey and Werdell, 2006; Hlaing et al., 2013; Jamet et al., 2011; Zibordi et al., 2009a). In this study, because our measurements were mostly from nearshore complex waters (Fig. 1) where the water depth and bottom benthic type may change drastically over a very short distance, the satellite R_{rs} from the center pixel (*i.e.*, 1×1) of the Landsat-8 images closest to an *in situ* site was used for subsequent analysis, rather the conventional average of a 3×3 box.

Several metrics were adopted to evaluate the matchups, including the relative root-mean square deviation (rRMSD), bias, mean absolute percentage difference (MAPD) and unbiased or symmetric mean absolute percentage deviation (SMAPD), expressed as

$$rRMSD = \sqrt{\frac{1}{N} \sum_{i=1}^N \left[\frac{S_{i,1} - S_{i,2}}{S_{i,2}} \right]^2} \times 100\% \quad (7)$$

$$bias = \text{median}\{(S_{i,1} - S_{i,2})/S_{i,2} \times 100\% \} \quad (8)$$

$$MAPD = \frac{1}{N} \sum_{i=1}^N |(S_{i,1} - S_{i,2})/S_{i,2}| \times 100\% \quad (9)$$

$$SMAPD = \frac{2}{N} \sum_{i=1}^N \left| \frac{S_{i,1} - S_{i,2}}{S_{i,1} + S_{i,2}} \right| \times 100\% \quad (10)$$

where $S_{i,1}$ and $S_{i,2}$ refer to the satellite products and *in situ* measurements under investigation, respectively, and N the number of data pairs.

The cosine distance was derived to quantify the spectral similarity between satellite and *in situ* R_{rs} spectra (*e.g.* Wei et al., 2016),

$$\cos \alpha = \sum_{i=1}^N [S_{i,1} \cdot S_{i,2}] / \sqrt{\sum_{i=1}^N [S_{i,1}]^2 \sum_{i=1}^N [S_{i,2}]^2} \quad (11)$$

where α is the angle formed between the spectra $S_{i,1}$ and $S_{i,2}$.

In addition, the QA scores (Wei et al., 2016) were calculated to evaluate the data quality of Landsat-8 R_{rs} spectra. Here the original quality assurance system was adapted for the four wavelengths and their wide bandpasses of the OLI instrument (accessible at http://oceanoptics.umb.edu/score_metric). The QA score system is designed specifically for optically deep aquatic environments. Therefore, in the following analysis, it was only applied to the satellite measurements in turbid waters of Massachusetts Bay and Boston Harbor. It is emphasized that the QA system relies on the R_{rs} reference spectra to represent the spectral similarity and the upper and lower constraining spectra to define the range of variability. There are no gaps in the domain of coverage from purple-blue waters to yellow turbid waters. Some exceptional cases do exist and may not be included in the current QA system, such as the waters with blooms or oil slicks. However, such outliers were not observed at our study sites. Based on the total number of available wavelengths with OLI instrument, five levels of quality scores (0, 0.25, 0.5, 0.75 and 1) were quantified and used in the analysis of R_{rs} quality.

3. Results

3.1. In situ R_{rs} spectra in coral reefs and turbid coastal waters

The *in situ* hyperspectral R_{rs} spectra are plotted for these optically contrasting waters separately in Fig. 3. These spectra are representative of the light field with moderate solar zenith angles, 25–45° and 40–60° for coral reefs and turbid waters, respectively. The coral reef waters are optically shallow, and the R_{rs} spectra are significantly impacted by bottom contributions. As shown in Fig. 3A, the R_{rs} spectra in such

environments vary over a wide range of magnitudes and spectral shapes. At the green bands, for instance, R_{rs} can be as high as 0.055 sr^{-1} in sandy patches, while it can be as low as 0.005 sr^{-1} over macroalgae- and/or corals-dominated substrates. The coral reef waters are generally very clear (refer to Section 2.1). Depending on the water clarity, depth and bottom reflectance, the maxima of R_{rs} spectra vary within a wide spectral domain between 475 and 575 nm. The turbid waters in Boston Harbor and Massachusetts Bay are optically deep, where the contribution of bottom to R_{rs} is negligible. The R_{rs} spectra from these turbid waters generally peak in the green domain and also exhibit a typical fluorescence peak around 685 nm (Fig. 3B). Note that the magnitudes of R_{rs} spectra from the Harbor generally do not exceed 0.015 sr^{-1} , while the R_{rs} spectra from the Bay are much lower in magnitude (as low as 0.002 sr^{-1} at 561 nm) due to elevated absorption-to-scattering ratios of water constituents.

3.2. Landsat-8 R_{rs} product quality in coral reef waters

As stated earlier, the satellite R_{rs} products in coral reef environments have rarely been evaluated due to the lack of appropriate *in situ* matchup data. Our extensive field measurements allow a first comprehensive performance analysis for such shallow environments. Visual observation indicates qualitative consistence between the Landsat-8 R_{rs} spectra (Fig. 4) and *in situ* data (Fig. 3). However, there exist a few

questionable spectra, such as the negatively biased spectra with Acolite/SWIR (Fig. 4B) and Acolite/NIR (Fig. 4C) and underestimated bright target spectra with CSA (Fig. 4D). According to the cosc metric, the R_{rs} products from NASA algorithm exhibit the highest spectral similarity (with high cosc values) to the *in situ* matchup spectra (Table 3). It is noticeable that the NASA products have fewer available matchups ($N = 27$) when compared to those of Acolite and CSA products ($N = 34$). This is mostly due to the missing Thermal Infrared Sensor (TIRS) data in one Landsat-8 image (LO80050482015063, in Table 1), which are required by SeaDAS (v7.4).

The scatter plots between *in situ* and satellite matchup R_{rs} of shallow coral reef environments are shown in Fig. 5. Among the four comparisons, the NASA products exhibited the smallest biases from the *in situ* data, with a linear slope close to 1:1 line and $R^2 = 0.77$. In contrast, the CSA products have a much larger deviation from 1:1 with a smaller R^2 , partly due to the significantly underestimated R_{rs} for a few brighter targets where the *in situ* R_{rs} at blue and green bands is $> 0.02 \text{ sr}^{-1}$ (Fig. 5D). In this regard, the Acolite products have exhibited moderate performance (Fig. 5B and Fig. 5C). According to other criteria including bias, MAPD and rRMSD, the best overall performance is achieved by the NASA approach, with MAPD $\approx 25\%$ and rRMSD $\approx 33\%$ in the blue-green domain (Table 3). The Acolite/NIR and CSA products have moderate performance in these R_{rs} products with MAPD of $\sim 29\%$ and $\sim 33\%$, respectively, and rRMSD of 37% and 43%, respectively. The R_{rs}

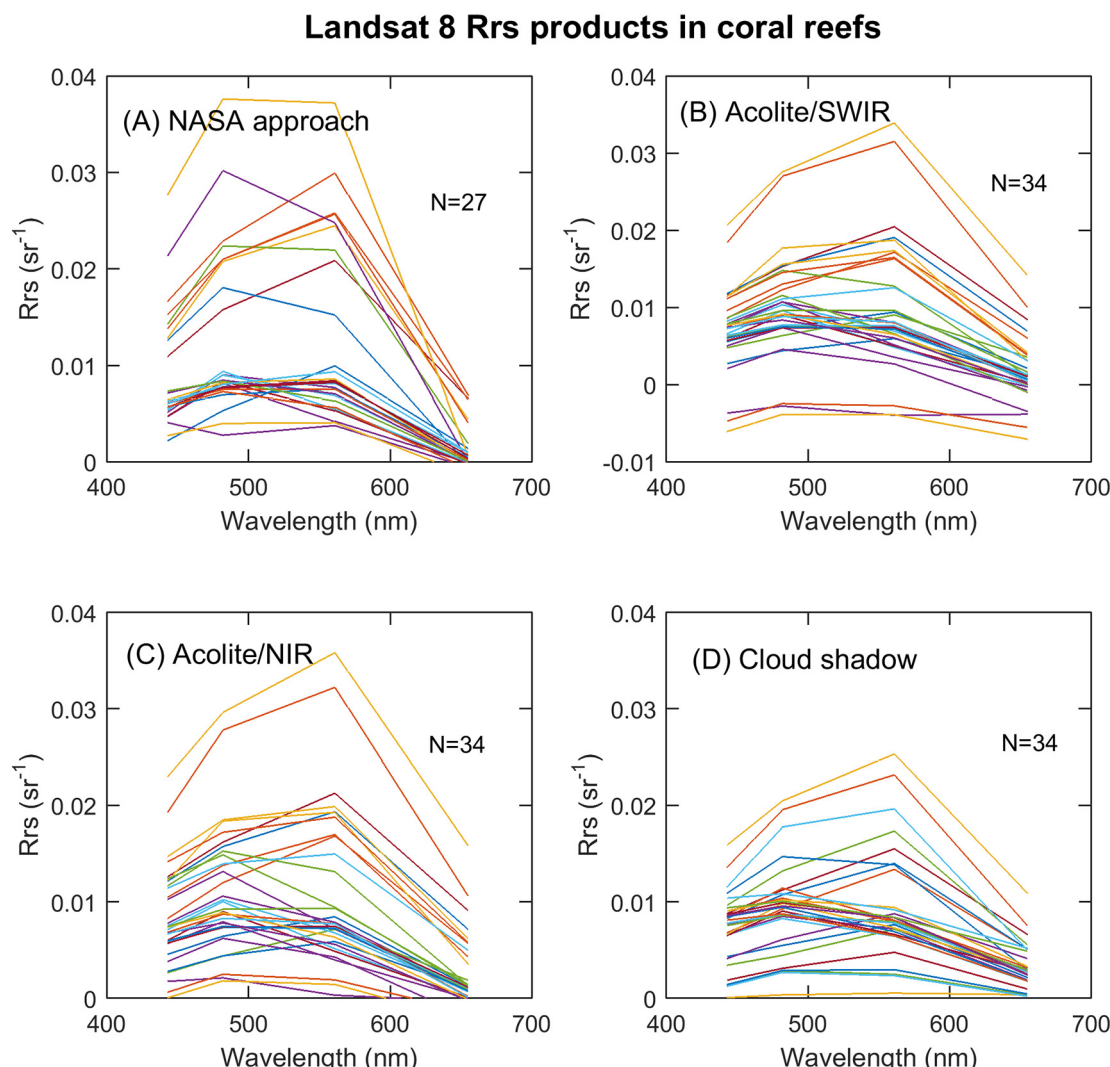


Fig. 4. Landsat-8 R_{rs} spectra in shallow coral reef environments derived from (A) NASA approach, (B) Acolite/SWIR, (C) Acolite/NIR, and (D) cloud-shadow approach.

Table 3

Statistical results for the remote sensing reflectance matchup data derived from the NASA, Acolite/SWIR, Acolite/NIR and CSA methods in specific water types. For each band the best performance is rendered in bold face. The values within the parentheses refer to the standard deviations.

	λ	Coral reefs					Turbid waters					
		bias	MAPD	rRMSD	cosa	N	bias	MAPD	rRMSD	cosa	Mean QA scores	N
NASA standard method	443	-2%	24%	34%	0.99	27	-25%	59%	74%	0.96	0.79	18
	482	1%	25%	33%	(0.02)		-2%	36%	48%	(0.08)	(0.30)	
	561	-13%	25%	31%			-1%	18%	24%			
	655	-79%	87%	109%			-2%	41%	59%			
Acolite/SWIR	443	-7%	34%	54%	0.83 (0.51)	34	116%	181%	246%	0.96	0.70	23
	482	-5%	32%	47%			65%	107%	142%	(0.04)	(0.31)	
	561	-17%	37%	53%			17%	42%	55%			
	655	-44%	149%	323%			51%	131%	191%			
Acolite/NIR	443	-10%	29%	38%	0.97	34	19%	102%	130%	0.93	0.78	23
	482	-11%	28%	35%	(0.08)		7%	55%	72%	(0.11)	(0.29)	
	561	-19%	30%	38%			-15%	22%	26%			
	655	-51%	85%	138%			-18%	48%	83%			
Cloud shadow approach	443	-15%	36%	46%	0.98	34	12%	43%	63%	0.99	0.88	17
	482	-16%	33%	43%	(0.02)		3%	33%	45%	(0.01)	(0.18)	
	561	-16%	31%	41%			-18%	31%	39%			
	655	32%	133%	220%			32%	95%	175%			

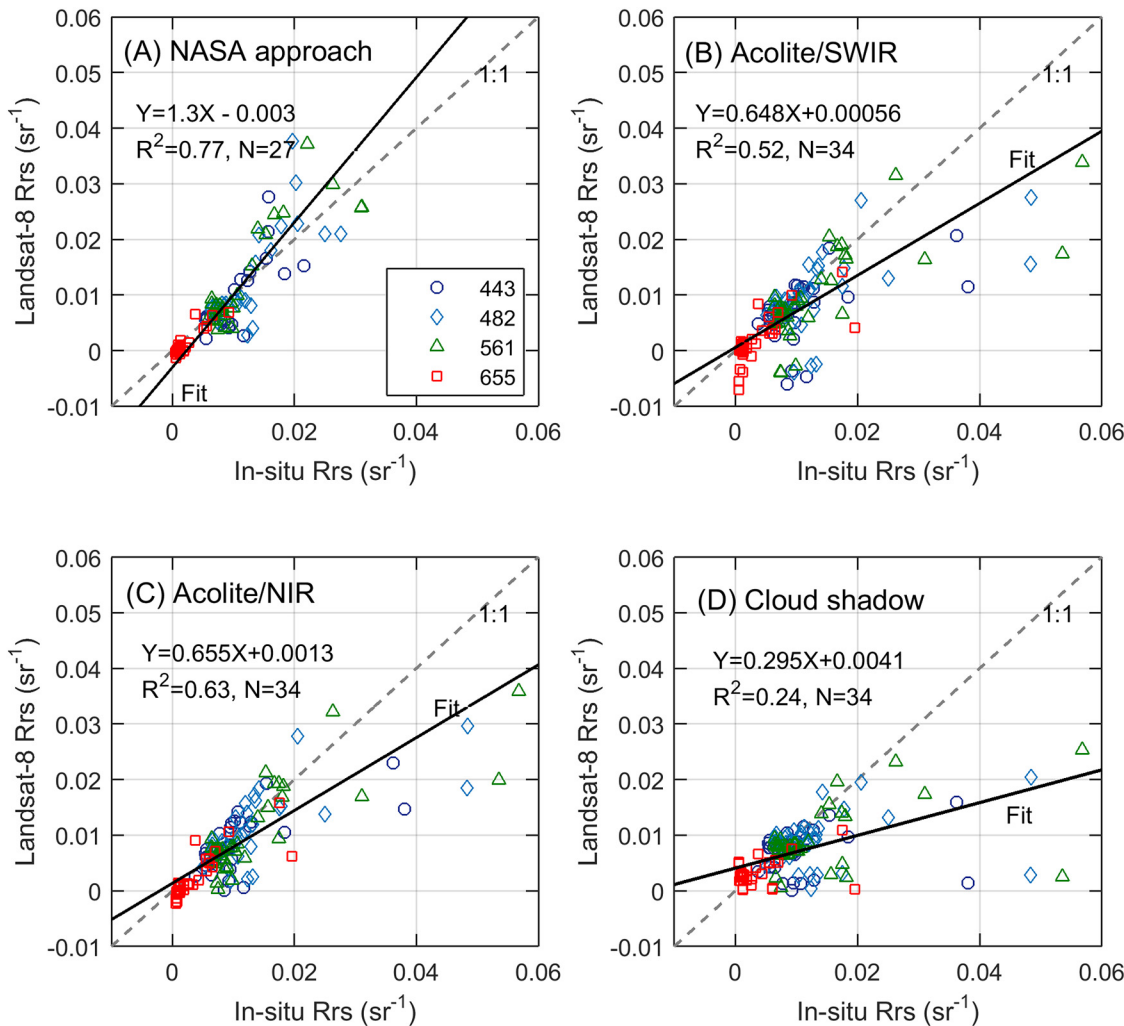


Fig. 5. Landsat-8 estimated $R_{rs}(\lambda)$ versus *in situ* data measured $R_{rs}(\lambda)$ at bands of 443, 482, 561, and 655 nm in the coral reef environments. The dash line refers to 1:1 line, and the black line represents the linear regression with the fitting parameters given in the plots. The legend given in (A) also applies to subplots (B), (C) and (D).

products of Acolite/SWIR have the largest deviations from *in situ* measurements with MAPD = 34% and rRMSD = 51%, respectively. Also, the assessment indicates that the NIR approach is slightly advantageous over the SWIR approach as implemented by Acolite, likely

because of the low signal-to-noise ratios at SWIR bands. Without exception, relatively larger differences are observed at the red band, mainly because the R_{rs} values at this band are usually small (with a median value 0.0013 sr^{-1}) in these waters (see Fig. 3A).

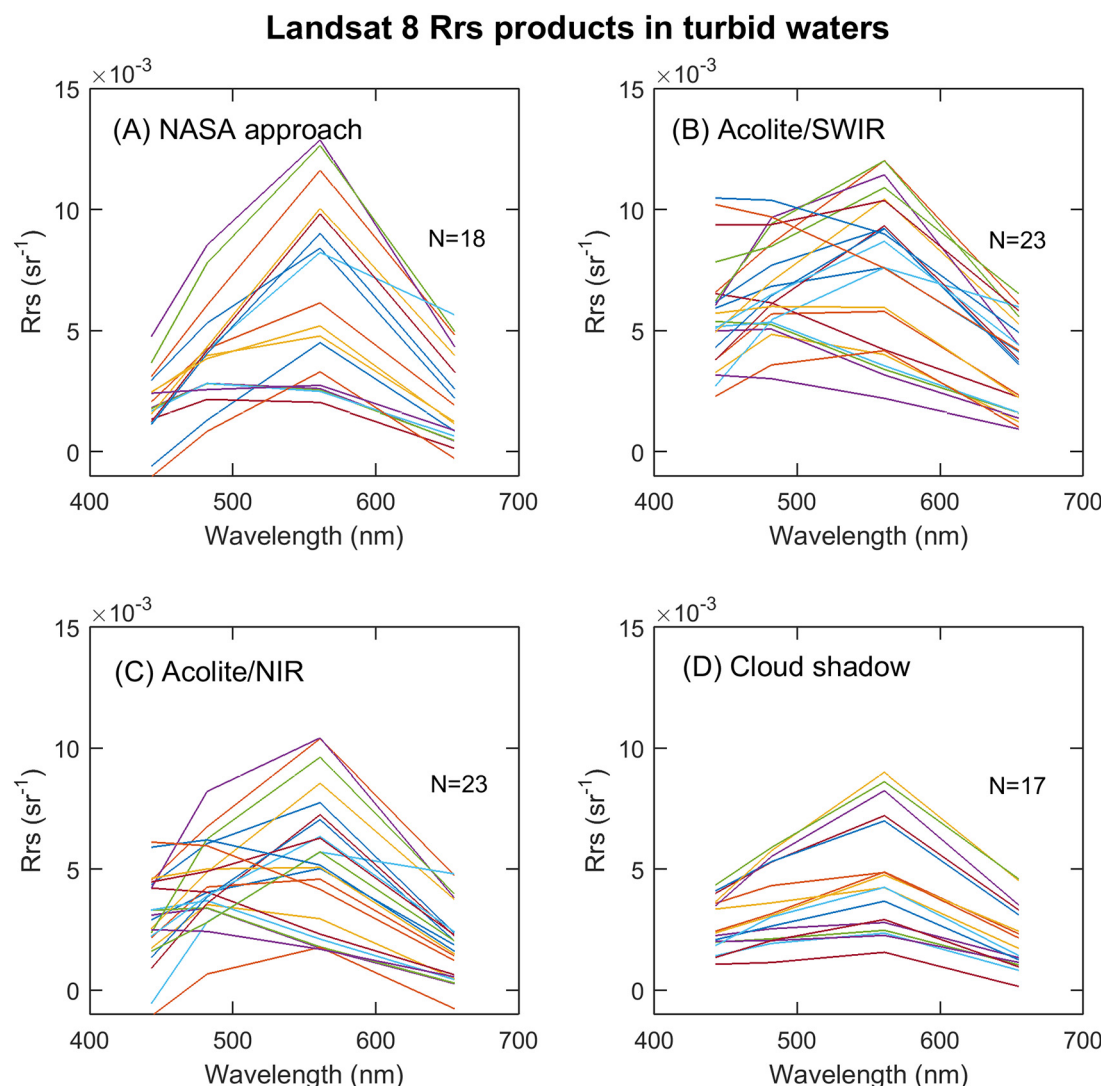


Fig. 6. Landsat-8 R_{rs} spectra in optically deep turbid waters of Massachusetts Bay and Boston Harbor derived from (A) NASA approach, (B) Acolite/SWIR, (C) Acolite/NIR, and (D) cloud-shadow approach.

It is noted that Acolite and NASA approaches have generated negative R_{rs} values at certain bands. The NASA negative products are only found at 655 nm band. For Acolite products, negative data could be at the blue (443 nm), green and red bands. Statistically, the NASA approach has the highest appearance of negative $R_{rs}(655)$ products (26%, Fig. 5A), while the Acolite products have slightly fewer negative values at the red band, 23% for Acolite/SWIR (Fig. 5B) and 18% for Acolite/NIR (Fig. 5C). Such negative data products are likely a result of inaccurate determination of the aerosol types and/or inherently low R_{rs} values at such red band.

3.3. Landsat-8 R_{rs} product quality in turbid waters

Besides the analyses in the coral reefs, we evaluated the R_{rs} products in the optically deep waters of Massachusetts Bay and Boston Harbor. The Landsat-8 R_{rs} spectra from the matchup stations are displayed in Fig. 6. Among all the products, the R_{rs} spectra from CSA show no obvious sign of quality problems. According to the spectral similarity parameter cosca, the CSA products have generated the best R_{rs} spectra (Table 3). The fewer matchup data for NASA products were a result of the change to the Landsat-8 data inventory structure in April 2017, which made SeaDAS (v7.4) unable to handle the new data structure. Besides which, no clouds were found in two of the Landsat-8 images

over Massachusetts Bay, leading to fewer matchups for the CSA approach than Acolite products.

Fig. 7 further illustrates relationships between these *in situ* and satellite matchup R_{rs} data and Table 3 provides the validation statistics. Based on these evaluations, strong agreement is found for the data products from NASA and CSA approaches. They both exhibit fairly good performance in blue-green domain with MAPD = 18–59% and 31–43%, respectively, and rRMSD = 24–74% and 39–63%, respectively. It is notable that such a performance is close to that of the operational satellite ocean color sensors in complex coastal waters (Hlaing et al., 2013; Zibordi et al., 2009a). It is also interesting to note that the NASA approach has resulted in systematically underestimated R_{rs} values, echoing the results observed at AERONET-OC sites (Pahlevan et al., 2017).

As with the observations in the coral reefs, the Acolite products in optically deep waters exhibit slightly larger differences and biases than the NASA and CSA products, but fewer negative data points compared to the shallow water matchups. Although the Acolite/SWIR and *in situ* matchups are closer to the 1:1 line, Acolite/NIR products have shown higher accuracy with smaller MAPD and rRMSD.

The average QA scores (with the standard deviations) are provided in Table 3. From this independent criterion, the CSA products are the most reasonable with the highest QA score of 0.88, followed by NASA

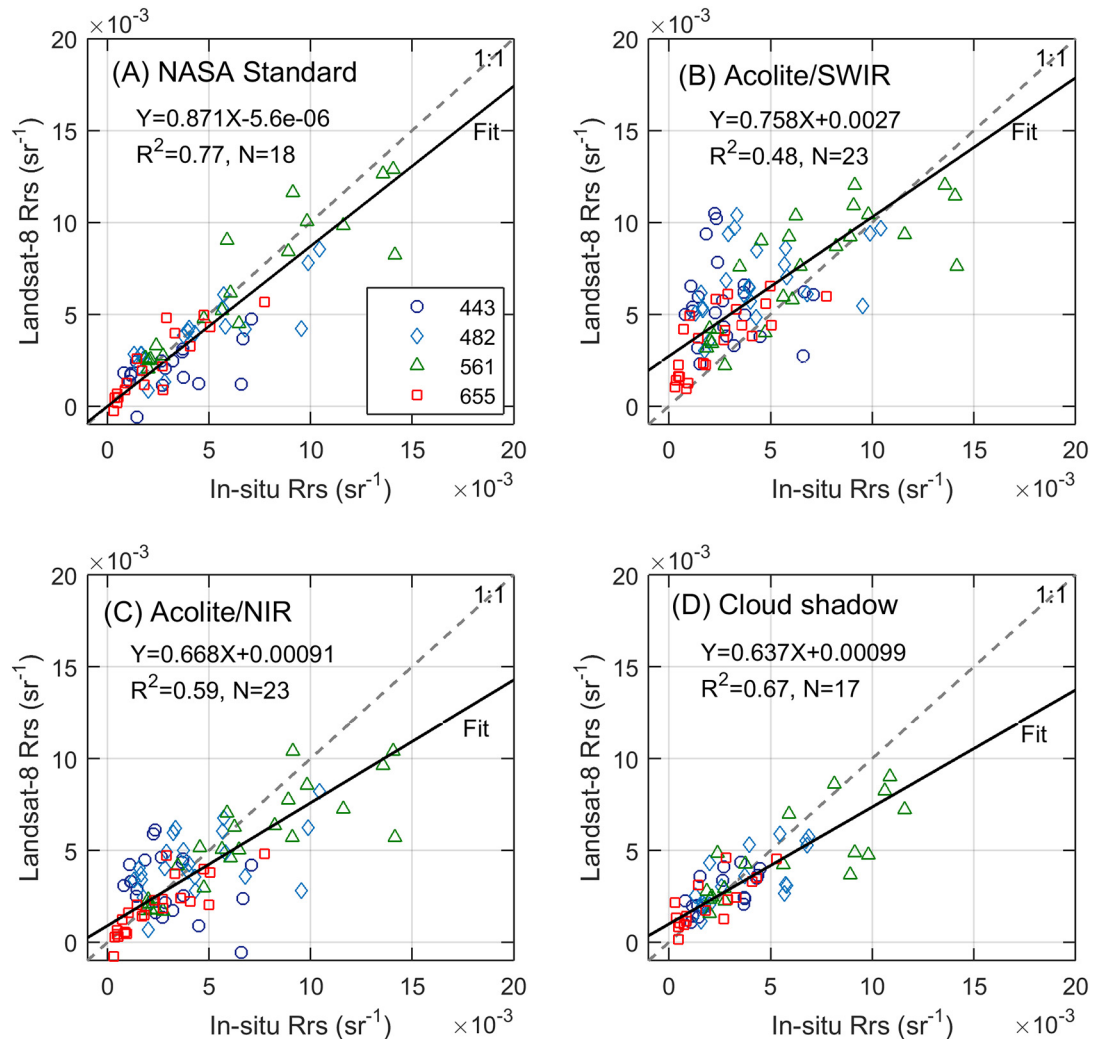


Fig. 7. Landsat-8 estimated $R_{rs}(\lambda)$ versus *in situ* data measured $R_{rs}(\lambda)$ at bands of 443, 482, 561, and 655 nm in Massachusetts Bay and Boston Harbor. The dash line refers to 1:1 line, and the black line represents the linear regression with the fitting parameters given in the plots. The legend in (A) also applies to (B), (C) and (D).

products with a QA score of 0.79. The Acolite/NIR products are generally more reasonable with higher QA scores than the Acolite/SWIR products. These scoring results are in concert with the R_{rs} matchup evaluations obtained in this study, supporting that the QA scores can be used as an independent measure for quantitative evaluation of the Landat-8 R_{rs} product quality.

3.4. Overall evaluation of Landsat-8 R_{rs} data products

To characterize the performance of each atmospheric correction scheme, we combined all available matchups from optically deep and shallow waters in previous sections and further assessed the overall R_{rs} product quality. It is found that the NASA and *in situ* matchups are the closest to the 1:1 line with $R^2 = 0.79$ (Fig. 8A). Based on the validation metrics and spectral similarity, the NASA standard approach has also shown the highest performance, immediately followed by the CSA approach and Acolite/NIR across both deep and shallow waters (Table 4). Specifically, the MAPD's vary between 23 and 33% and 31–38% in blue-green domain for the NASA and CSA products, respectively. The Acolite/SWIR products show slightly lower performance, particularly at blue bands. The lower performance of Acolite/SWIR products, as indicated by the present datasets, is probably because of the low signal-to-noise ratios of the SWIR bands which were not specifically designed for the typical radiances encountered over these water bodies and the biases associated with the aerosol determinations.

4. Discussion

4.1. Validation uncertainty

Among the four atmospheric correction schemes, the SeaDAS and Acolite systems require accurate knowledge of aerosol types to obtain high quality R_{rs} retrievals (Franz et al., 2015; Vanhellemont and Ruddick, 2014, 2015). The two systems employ different mechanisms for aerosol determination (Section 2.3), which have played a role in their performance as manifested in the matchup analyses (Section 3). Yet, the uncertainties associated with the aerosol determinations are generally unknown. The CSA approach is image based and still requires user decision during the data processing (Lee et al., 2007). It does not need profound radiative transfer knowledge and absolute calibration of the sensor. Furthermore, it is easy to implement. However, this image-based procedure requires the radiance from cloud shadows over waters as input, which may not always be present, thereby limiting to some degree its applicability. Although the CSA retrievals are not significantly sensitive (< 10%) to the random selection of shadow, sunlit or cloud pixels (Lee et al., 2007; Zhang et al., 2017), the procedure proposed in this study relies on coincident measurements from the SNPP VIIRS satellite for the determination of cloud reflectance. In fact, other remote sensors can also be used for this purpose, including the recently launched VIIRS onboard NOAA-20 satellite and the Ocean and Land Color Instrument (OLCI) onboard Sentinel-3 satellite, which

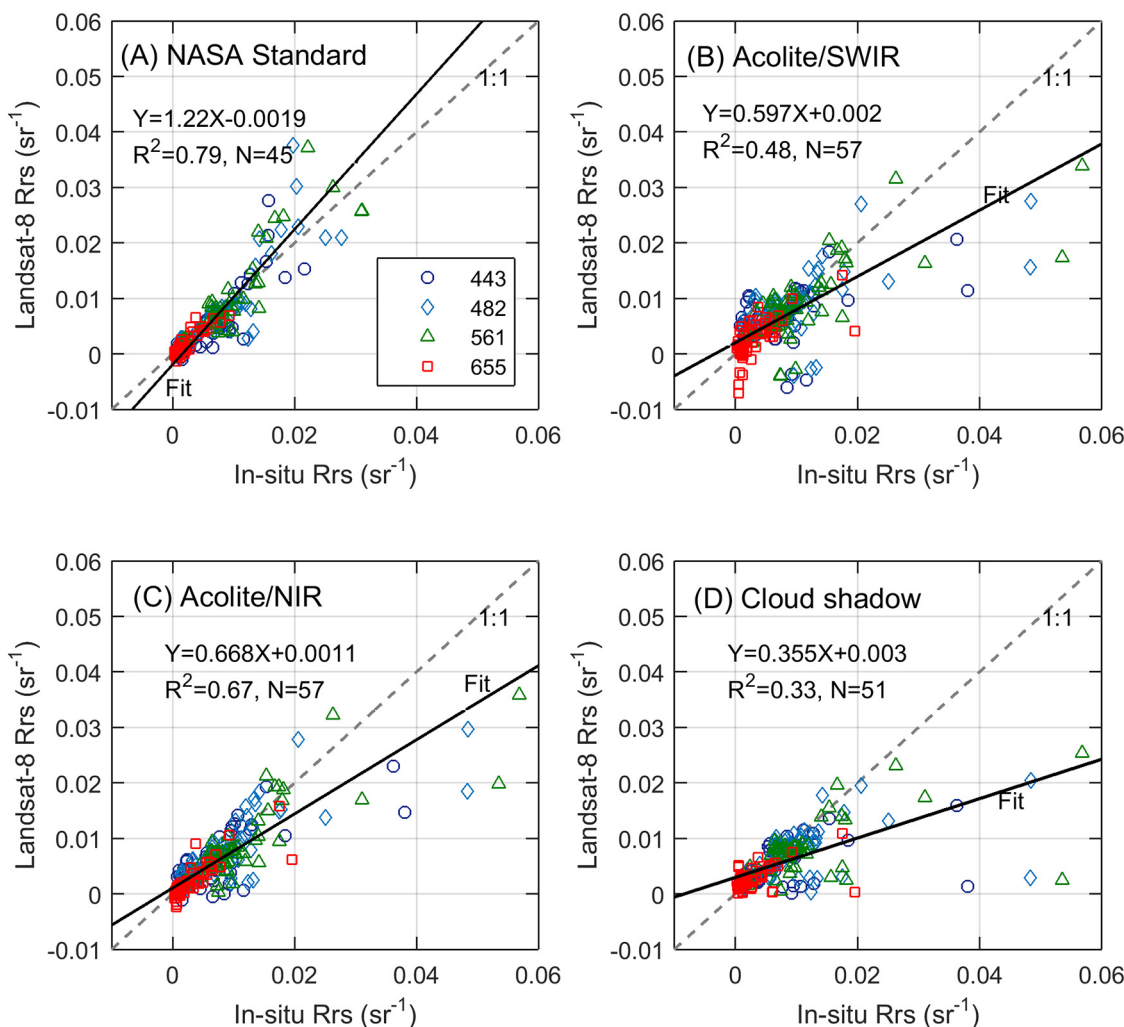


Fig. 8. Landsat-8 estimated $R_{rs}(\lambda)$ versus in situ data measured $R_{rs}(\lambda)$ at bands of 443, 482, 561, and 655 nm with all available matchup pairs. The dash line refers to 1:1 line, and the black line represents the linear regression with the fitting parameters given in the plots. The legend in (A) also applies to (B), (C) and (D).

Table 4

Statistical results for the remote sensing reflectance matchup data derived from the NASA, Acolite/SWIR, Acolite/NIR and CSA methods. For each band the best performance is rendered in bold face. The values within the parentheses refer to the standard deviations.

λ	Coral reefs & Turbid waters				
	bias	MAPD	rRMSD	cos α	N
NASA standard method	443	-8%	33%	43%	0.98
	482	-3%	30%	40%	(0.05)
	561	~0%	23%	29%	
	655	-21%	42%	50%	
Acolite/SWIR	443	4%	93%	162%	0.88
	482	12%	62%	97%	(0.39)
	561	-9%	39%	54%	
	655	-13%	142%	277%	
Acolite/NIR	443	-6%	59%	88%	0.96
	482	-2%	38%	53%	(0.10)
	561	-19%	27%	34%	
	655	-34%	70%	119%	
CSA	443	-11%	38%	52%	0.98
	482	-10%	33%	44%	(0.10)
	561	-17%	31%	41%	
	655	32%	121%	206%	

together allow for important overlap in observational coverage.

Besides the AC procedures, the on-orbit calibration of satellite ocean color sensors is critical for accurate R_{rs} retrievals at the water's surface. As the water-leaving radiance is only about 10% of the TOA radiance (Gordon and Wang, 1994), a small radiance measurement error at the TOA can propagate to L_w and R_{rs} at the water surface as a much larger error. Pahlevan et al. (2014) and Franz et al. (2015) derived vicarious calibration gains for OLI's seven bands (443, 482, 561, 655, 865, 1606 and 2201 nm). The former is based on MODTRAN® radiative transfer simulation, while the latter is developed specifically for SeaDAS. The sensitivity of the Landsat-8 R_{rs} retrieval to the selection of vicarious gains was investigated for the SeaDAS and Acolite system. Application of the vicarious calibration gains of Pahlevan et al. (2014) leads to slightly improved agreement for the R_{rs} matchup data, with smaller MAPD's and rRMSD's at most of the bands than those with Franz et al. (2015) (Table 5) and those without vicarious calibration (Table 4). However, the gains of Pahlevan et al. (2014) also cause overly underestimated R_{rs} products at the deep blue band for SeaDAS. In general, as indicated by the comparisons here, the NASA approach has generated more reliable R_{rs} products.

The remotely sensed R_{rs} products in the vicinity of land environments can be biased due to the adjacency effect caused by complicated

Table 5

Statistical results for the remote sensing reflectance matchup data (coral reefs & turbid waters) after applying the vicarious calibration gains to the TOA radiance. Refer to Table 4 for CSA retrievals.

	λ	Gains of Franz et al. (2015)				Gains of Pahlevan et al. (2014)			
		bias	MAPD	rRMSD	cosa	bias	MAPD	rRMSD	cosa
NASA standard method	443	8%	43%	61%	0.98	−49%	49%	59%	0.97
	482	26%	43%	65%		1%	25%	35%	
	561	1%	23%	30%		−3%	22%	28%	
	655	−27%	60%	80%		−21%	57%	71%	
	Acolite/SWIR	33%	116%	196%	0.95	−2%	71%	123%	0.92
Acolite/NIR	443	33%	116%	196%	0.95	19%	59%	92%	
	482	42%	87%	131%		−2%	33%	47%	
	561	7%	35%	50%		14%	113%	200%	
	655	20%	116%	202%		−36%	59%	74%	0.93
	Acolite/NIR	5%	63%	102%	0.96	−13%	35%	47%	
	482	18%	49%	73%		−24%	29%	36%	
	561	−14%	26%	33%		−40%	71%	118%	
	655	−24%	64%	111%					

multiple scattering in the atmosphere-land system (Santer and Schmechtig, 2000). Correction of these biases requires accurate knowledge of land topography, surface albedo and aerosols over land, etc. It is operationally difficult to implement and so was not included in any of the AC schemes examined in this study.

BRDF effect partly contributes to the difference between satellite and *in situ* R_{rs} products. To further understand the validation uncertainty, we reprocessed the deep water Landsat-8 images with SeaDAS by turning on the BRDF correction. It is found that the BRDF-corrected R_{rs} products differ by ∼5% on average from the BRDF-uncorrected R_{rs} products, with SMAPD = 3%, 5%, 6% and 4% for the bands of 443, 482, 561 and 655 nm, respectively (refer to Eq. (10)). These differences are quite small comparing with the MAPD's given in Fig. 3, suggesting that the current operational BRDF algorithm in SeaDAS does not improve the validation results considerably, at least for these datasets. After all, the BRDF algorithm of Morel et al. (2002) is optimized and most suitable for typical oceanic waters.

We further evaluated the uncertainty of *in situ* R_{rs} based on the coefficient of variation (CV), which was derived as the ratio of the standard deviation to mean of all R_{rs} spectra measured over the period of 3–5 min and after passing through the filtering procedures (see Section 2.2). In Massachusetts Bay and Boston Harbor, the CV's for R_{rs} measurements are generally < 5%, specifically 4.5%, 4.1%, 3.6% and 5% at bands of 443, 482, 561 and 655 nm, respectively. These statistics are comparable with earlier reports (Lee et al., 2013; Wei et al., 2015), suggesting highly stable *in situ* R_{rs} measurements. In the coral reefs, the coefficient of variation is slightly higher (7.9%, 8.4%, 7.8% and 7.5% at the same four bands), partly a result of the bottom heterogeneity. For either situation, these measurement uncertainties are far below those of matchup data as shown in this study (Table 3 and Table 4).

The satellite R_{rs} spectra are often averaged over a box of some number of pixels for matchup analysis (Bailey and Werdell, 2006; Hlaing et al., 2013; Zibordi et al., 2009a). In practice, if the CV of valid pixels within the defined box is < 15%, the satellite R_{rs} retrievals will be included for further analysis (Bailey and Werdell, 2006). The Landsat-8 R_{rs} measurements in coral reefs are, however, highly variable in the spatial domain. As a consequence of the spatial heterogeneity, the CV of a box of 3 × 3 pixels can be much higher than 15% at all four wavelengths (Table 6). For the turbid waters of Boston Harbor and Massachusetts Bay, $R_{rs}(482)$ and $R_{rs}(561)$ measurements exhibit limited spatial variability, but large CV is still observable at 443 and 655 nm (Table 6). The large spatial variation revealed in our Landsat-8 measurements does not support the conventional spatial averaging for matchup validation. Such large spatial variability in Landsat-8 R_{rs} retrievals also contributes to the observed matchup uncertainty in Table 3 and Table 4.

Based on results from these analyses, reliable R_{rs} products can be

Table 6

Coefficient of variation of Landsat-8 R_{rs} measurements (processed by SeaDAS v7.4) at the matchup sites (calculated over 3 × 3 pixel neighborhood) with the mean CV given in parentheses.

	443	482	561	655
Coral reefs: Puerto Rico	4–210% (31%)	3–129% (20%)	3–164% (23%)	5–153% (56%)
Coral reefs: Florida Keys	6–26% (17%)	6–25% (17%)	7–20% (15%)	43–135% (63%)
Coral reefs: Maui	5–121% (24%)	5–85% (19%)	4–55% (15%)	1–159% (75%)
Boston Harbor	7–49% (23%)	4–31% (11%)	2–14% (5%)	3–157% (23%)
Massachusetts Bay	16–20% (19%)	7–11% (10%)	6–10% (9%)	20–52% (36%)

achieved from Landsat-8 in various waters (Table 3), despite the instrument's lower signal-to-noise ratios comparing to other operational ocean color satellites. Considering all the challenges discussed above, the agreement between matchups, particularly of those from CSA and NASA approach, are strong. The R_{rs} product accuracy in blue-green bands (MAPD = 21–60% and 31–43%, respectively) are even close to those obtained by operational ocean color sensors in coastal waters (Hlaing et al., 2013; Jamet et al., 2011; Zibordi et al., 2009a). With high spatial resolution, the accurate Landsat-8 R_{rs} measurements can be used in a variety of aquatic applications.

4.2. Impacts on water optical property retrievals and reflectance band ratios

The measurement uncertainties in the satellite R_{rs} products can impact the subsequent ocean color retrievals derived from analytical or semi-analytical algorithms (Goodman et al., 2008; Lee et al., 2010; Salama et al., 2011; Wei and Lee, 2015). We estimated the absorption coefficient (a_{pg}) due to particles and colored dissolved organic material (CDOM) and the particle backscattering coefficient (b_{bp}) with Landsat-8 satellite R_{rs} data and *in situ* R_{rs} measurements, respectively, using a semi-analytical algorithm developed for Landsat-8 for deep waters (Lee et al., 2016). Comparisons of the SMAPD's between satellite and *in situ* retrievals indicate that the CSA products allow more reliable estimation of a_{pg} , while the b_{bp} estimation from NASA products is more accurate (Fig. 9).

For some empirical algorithms using R_{rs} band ratios, the absolute accuracy of R_{rs} products may not play a primary role in determining subsequent ocean color products. Rather, the ratios of reflectance are important, as quantified by the metric, cosa. For instance, they can be used for the estimation of chlorophyll *a* concentrations in optically deep waters (O'Reilly et al., 1998) or the derivation of shallow-water

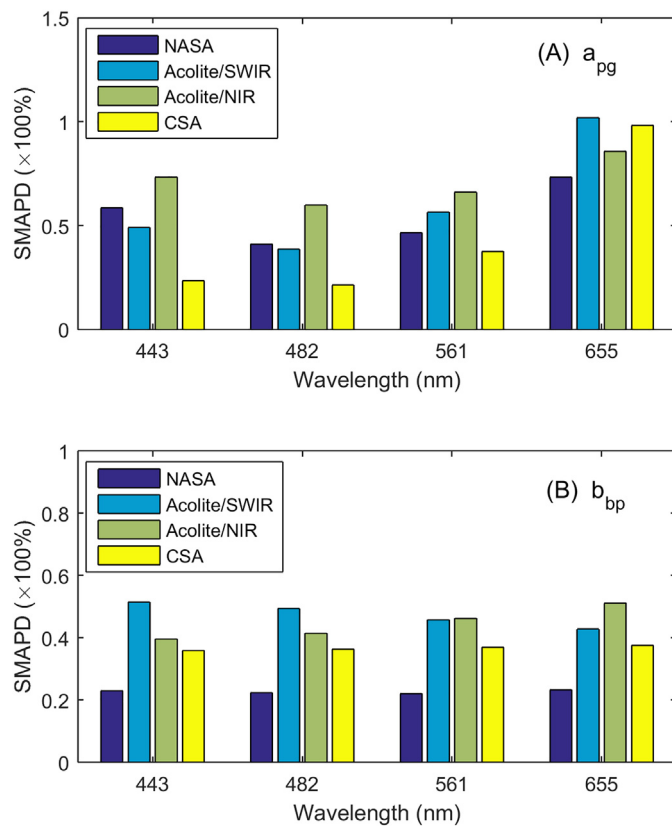


Fig. 9. Relative uncertainty of the model-derived properties of (A) a_{pg} and (B) b_{bp} with the Landsat-8 Rrs spectra and *in situ* measurement Rrs spectra.

bathymetry (Stump et al., 2003). We provided examples for such band-ratio comparisons in Fig. 10 between Landsat-8 and *in situ* data. The NASA products have the smallest deviations in coral reefs, while the CSA products are more accurate in deep waters – an observation that is consistent with the cosa metric in Table 3 and Table 4.

4.3. Independent assessment of Landsat-8 R_{rs} data quality

As discussed in this study, it is difficult to obtain *in situ* matchups with Landsat-8 measurements, especially because of its 16-day overpass and relatively small spatial coverage (185 km swath). Yet, it is

important to index the quality of each individual Landsat-8 R_{rs} spectrum for various ocean color retrievals. Based on results in Table 3, the QA scores provide an independent quantification for the quality of R_{rs} spectra. When applied to Landsat-8 images, the QA scores may further provide insights into the overall quality of the satellite R_{rs} data as well as potential spatial variability. To visualize the effectiveness of this metric, the QA scores were derived for the R_{rs} products of one selected image generated from four atmospheric correction schemes. According to the comparisons, the CSA and NASA products show generally higher data quality, with an average QA score of 0.73 and 0.60, respectively (Fig. 11D and Fig. 11A), while the Acolite/SWIR and Acolite/NIR products have quality scores of 0.50 and 0.45, respectively (Fig. 11B and Fig. 11C). Besides, the spatial variability of R_{rs} data quality is clearly revealed in the QA score maps. For instance, the CSA product shows very high QA scores in Massachusetts Bay (upper right of the image) while the three others suggest problematic retrievals in that region. Such contrasts are likely a consequence of the presence of absorbing aerosols in the air, which the NASA and Acolite algorithms cannot account for sufficiently. It is cautioned that the current QA system does not necessarily cover every type of waters occurring in nature. Exceptional cases do exist, for instance, blooms and oil slicks. So a valid R_{rs} spectrum might still be scored low if it happens to be an exceptional case and insufficiently represented by present QA system.

5. Conclusions

To assess the performance of Landsat-8 OLI R_{rs} products in aquatic environment, in particular coral reef systems, we have examined R_{rs} data products with radiative transfer-based and image-based atmospheric correction schemes. The R_{rs} products were validated with concurrent *in situ* measurements of hyperspectral R_{rs} data. Specifically, NASA's atmospheric correction scheme, the cloud-shadow approach and Acolite's NIR scheme generated R_{rs} products with strong agreement with *in situ* matchups in optically shallow waters. In the studied optically deep waters, NASA's approach and the cloud-shadow approach were found with the highest performance. According to all available matchups, the NASA and cloud-shadow approaches demonstrated overall the highest performance across coral reef environments and turbid waters. It is confirmed that high quality R_{rs} products can be achieved from the Landsat-8 satellite, supporting the application of Landsat-8 measurements in a variety of aquatic studies including coral reefs. Considering the complexity of natural waters and atmospheric conditions, validation of Landsat-8 OLI R_{rs} data over various waters is anticipated to be an ongoing task for the Landsat-8 science community.

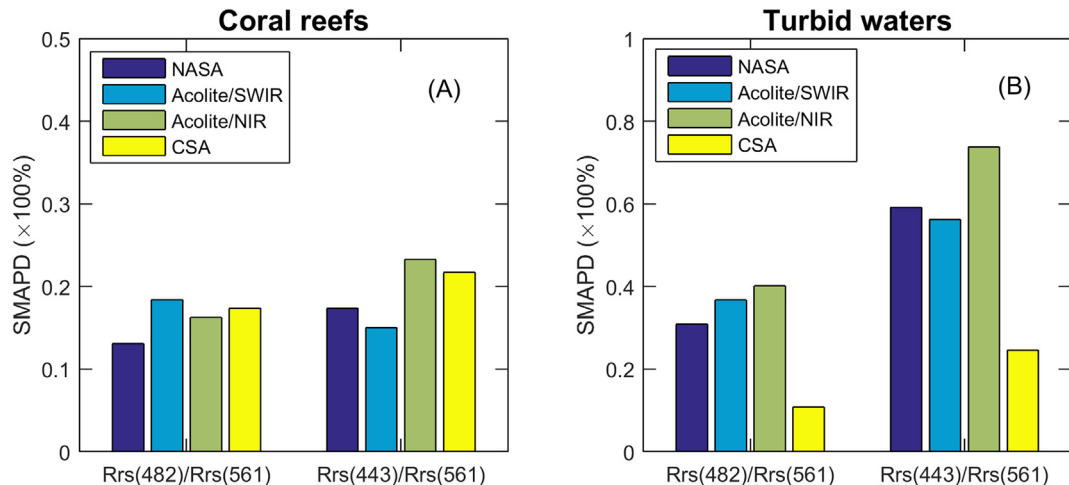


Fig. 10. The difference of R_{rs} blue-green band ratios between Landsat-8 matchups in (A) the shallow coral reefs, and (B) optically deep turbid waters.

Spatial variability of R_{rs} data quality (QA scores)

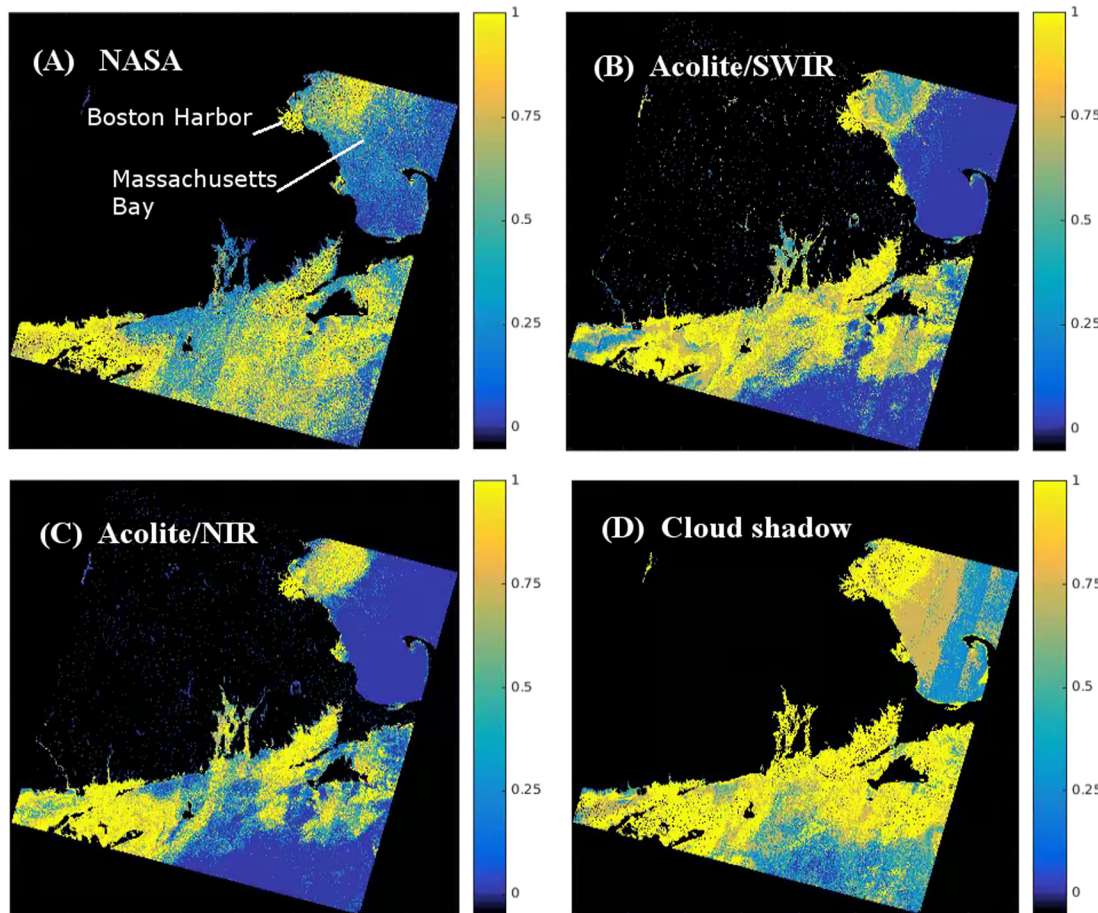


Fig. 11. Comparison of QA scores for the Landsat-8 R_{rs} products (LC80120312015240) derived from different atmospheric correction schemes: (A) NASA standard approach, (B) Acolite/SWIR, (C) Acolite/NIR, and (D) cloud-shadow approach.

Acknowledgements

The authors would like to thank USGS for the distribution of Landsat-8 Level-1 data products, the NASA Ocean Biology Processing Group for the development and support of the SeaDAS software, and Q. Vanhellemont and K. Ruddick for the development and support of the Acolite software. This study is co-funded by the USGS project, the NASA HypsIPI and CORAL projects (NNX15AR96G, NNX16AB05G), the NOAA JPSS VIIRS Ocean Color Cal/Val Project (NA11OAR4320199) and the NOAA MIT Sea Grant Project (2015-R/RC-140). We thank Nima Pahlevan, Junfang Lin, Kelly Luis and Francesco Peri for their assistance in field sampling. Three anonymous reviewers are thanked for their constructive comments and suggestions.

References

- Ahmad, Z., Franz, B.A., McClain, C.R., Kwiatkowska, E.J., Werdell, P.J., Shettle, E.P., Holben, B.N., 2010. New aerosol models for the retrieval of aerosol optical thickness and normalized water-leaving radiances from the SeaWiFS and MODIS sensors over coastal regions and open oceans. *Appl. Opt.* 49, 5545–5560.
- Amin, R., Lewis, D., Gould, R.W., Hou, W., Lawson, A., Ondrusek, M., Arnone, R., 2014. Assessing the application of cloud shadow atmospheric correction algorithm on HICO. *IEEE Trans. Geosci. Remote Sens.* 52, 2646–2653.
- Andréfouët, S., Muller-Karger, F.E., Hochberg, E.J., Hu, C., Carder, K.L., 2001. Change detection in shallow coral reef environments using Landsat 7 ETM+ data. *Remote Sens. Environ.* 78, 150–162.
- Bailey, S.W., Werdell, P.J., 2006. A multi-sensor approach for the on-orbit validation of ocean color satellite data products. *Remote Sens. Environ.* 102, 12–23.
- Bailey, S.W., Hooker, S.B., Antoine, D., Franz, B.A., Werdell, P.J., 2008. Sources and assumptions for the vicarious calibration of ocean color satellite observations. *Appl. Opt.* 47, 2035–2045.
- Bailey, S.W., Franz, B.A., Werdell, P.J., 2010. Estimation of near-infrared water-leaving reflectance for satellite ocean color data processing. *Opt. Express* 18, 7521–7527.
- Eplee, R.E., Robinson, W.D., Bailey, S.W., Clark, D.K., Werdell, P.J., Wang, M., Barnes, R.A., McClain, C.R., 2001. Calibration of SeaWiFS. II. Vicarious techniques. *Appl. Opt.* 40, 6701–6718.
- Franz, B.A., Bailey, S.W., Kuring, N., Werdell, P.J., 2015. Ocean color measurements with the operational land imager on Landsat-8: implementation and evaluation in SeaDAS. *J. Appl. Remote. Sens.* 9, 096070.
- Giardino, C., Bresciani, M., Cazzaniga, I., Schenk, K., Rieger, P., Braga, F., Matta, E., Brando, V., 2014. Evaluation of multi-resolution satellite sensors for assessing water quality and bottom depth of Lake Garda. *Sensors* 14, 24116.
- Goodman, J.A., Lee, Z.P., Ustin, S.L., 2008. Influence of atmospheric and sea-surface corrections on retrieval of bottom depth and reflectance using a semi-analytical model: a case study in Kaneohe Bay, Hawaii. *Appl. Opt.* 47, F1–F11.
- Gordon, H.R., Wang, M., 1994. Retrieval of water-leaving radiance and aerosol optical thickness over the oceans with SeaWiFS: a preliminary algorithm. *Appl. Opt.* 33, 443–452.
- Gregg, W.W., Carder, K.L., 1990. A simple spectral solar irradiance model for cloudless maritime atmospheres. *Limnol. Oceanogr.* 35, 1657–1675.
- Hlaing, S., Harmel, T., Gilerson, A., Foster, R., Weidemann, A.D., Arnone, R., Wang, M., Ahmed, S., 2013. Evaluation of the VIIRS ocean color monitoring performance in coastal regions. *Remote Sens. Environ.* 139, 398–414.
- Hlaing, S., Gilerson, A., Foster, R., Wang, M., Arnone, R., Ahmed, S., 2014. Radiometric calibration of ocean color satellite sensors using AERONET-OC data. *Opt. Express* 22, 23385–23401.
- IOCCG, 2010. In: Wang, M. (Ed.), *Atmospheric Correction for Remotely-sensed Ocean Color Products*. IOCCG, Dartmouth, Nova Scotia, Canada, pp. 78.
- Jamet, C., Loisel, H., Kuchinke, C.P., Ruddick, K., Zibordi, G., Feng, H., 2011. Comparison of three SeaWiFS atmospheric correction algorithms for turbid waters using AERONET-OC measurements. *Remote Sens. Environ.* 115, 1955–1965.
- Lee, Z.P., Casey, B., Arnone, R., Weidemann, A.D., Parsons, R., Montes, M.J., Gao, B.C., Goode, W., Davis, C.O., Dye, J., 2007. Water and bottom properties of a coastal environment derived from Hyperion data measured from the EO-1 spacecraft platform. *J. Appl. Remote. Sens.* 1 (011502).

- Lee, Z.P., Arnone, R., Hu, C., Werdell, P.J., Lubac, B., 2010. Uncertainties of optical parameters and their propagations in an analytical ocean color inversion algorithm. *Appl. Opt.* 49, 369–381.
- Lee, Z.P., Pahlevan, N., Ahn, Y.-H., Greb, S., O'Donnell, D., 2013. Robust approach to directly measuring water-leaving radiance in the field. *Appl. Opt.* 52, 1693–1701.
- Lee, Z.P., Shang, S., Qi, L., Yan, J., Lin, G., 2016. A semi-analytical scheme to estimate Secchi-disk depth from Landsat-8 measurements. *Remote Sens. Environ.* 177, 101–106.
- Loveland, T.R., Irons, J.R., 2016. Landsat 8: the plans, the reality, and the legacy. *Remote Sens. Environ.* 185, 1–6.
- Lymburner, L., Botha, E., Hestir, E., Anstee, J., Sagar, S., Dekker, A., Malthus, T., 2016. Landsat 8: providing continuity and increased precision for measuring multi-decadal time series of total suspended matter. *Remote Sens. Environ.* 185, 108–118.
- Markham, B., Barsi, J., Kvaran, G., Ong, L., Kaita, E., Biggar, S., Czapla-Myers, J., Mishra, N., Helder, D., 2014. Landsat-8 operational land imager radiometric calibration and stability. *Remote Sens.* 6, 12275–12308.
- Mélin, F., Zibordi, G., Berthon, J.-F., 2007. Assessment of satellite ocean color products at a coastal site. *Remote Sens. Environ.* 110, 192–215.
- Mikelsons, K., Wang, M., 2018. Interactive online maps make satellite ocean data accessible. *Eos* 99. <http://dx.doi.org/10.1029/2018EO095653>.
- Morel, A., Antoine, D., Gentili, B., 2002. Bidirectional reflectance of oceanic waters: accounting for Raman emission and varying particle scattering phase function. *Appl. Opt.* 41, 6289–6306.
- Olmanson, L.G., Bauer, M.E., Brezonik, P.L., 2008. A 20-year Landsat water clarity census of Minnesota's 10,000 lakes. *Remote Sens. Environ.* 112, 4086–4097.
- O'Reilly, J.E., Maritorena, S., Mitchell, B.G., Siegel, D., Carder, K.L., Garver, S., Kahru, M., McClain, C., 1998. Ocean color chlorophyll algorithms for SeaWiFS. *J. Geophys. Res.* 103, 24937–24953.
- Otero, E., Carberry, K.K., 2005. Chlorophyll a and turbidity patterns over coral reefs systems of La Parguera Natural Reserve, Puerto Rico. *Rev. Biol. Trop.* 53, 25–32.
- Pacheco, A., Horta, J., Loureiro, C., Ferreira, Ó., 2015. Retrieval of nearshore bathymetry from Landsat 8 images: a tool for coastal monitoring in shallow waters. *Remote Sens. Environ.* 159, 102–116.
- Pahlevan, N., Lee, Z.P., Wei, J., Schaaf, C.B., Schott, J.R., Berk, A., 2014. On-orbit radiometric characterization of OLI (Landsat-8) for applications in aquatic remote sensing. *Remote Sens. Environ.* 154, 272–284.
- Pahlevan, N., Sheldon, P., Peri, F., Wei, J., Shang, Z., Sun, Q., Chen, R.F., Lee, Z.P., Schaaf, C.B., Schott, J.R., Loveland, T.R., 2016. Calibration/validation of Landsat-derived ocean color products in Boston Harbor, In: The International Archives of the Photogrammetry. In: Remote Sensing and Spatial Information Sciences, XXIII ISPRS Congress. International Society for Photogrammetry and Remote Sensing (ISPRS), Prague, Czech Republic, pp. 1165–1168.
- Pahlevan, N., Schott, J.R., Franz, B.A., Zibordi, G., Markham, B., Bailey, S., Schaaf, C.B., Ondrusek, M., Greb, S., Strait, C.M., 2017. Landsat 8 remote sensing reflectance (Rrs) products: evaluations, intercomparisons, and enhancements. *Remote Sens. Environ.* 190, 289–301.
- Palandro, D.A., Andréfouët, S., Hu, C., Hallock, P., Müller-Karger, F.E., Dustan, P., Callahan, M.K., Kranenburg, C., Beaver, C.R., 2008. Quantification of two decades of shallow-water coral reef habitat decline in the Florida Keys National Marine Sanctuary using Landsat data (1984–2002). *Remote Sens. Environ.* 112, 3388–3399.
- Pittman, S.J., Hile, S.D., Jeffrey, C.F.G., Clark, R., Woody, K., Herlach, B.D., Caldow, C., Monaco, M.E., Appeldoorn, R., 2010. Coral Reef Ecosystems of Reserva Natural de La Parguera (Puerto Rico): Spatial and Temporal Patterns in Fish and Benthic Communities (2001–2007). NOAA/NOS/National Centers for Coastal Ocean Science, Silver Spring, MD, pp. 202.
- Prouty, N.G., Cohen, A., Yates, K.K., Storlazzi, C.D., Swarzenski, P.W., White, D., 2017. Vulnerability of coral reefs to bioerosion from land-based sources of pollution. *J. Geophys. Res. Oceans* 122, 9319–9331.
- Qiu, Z., Xiao, C., Perrie, W., Sun, D., Wang, S., Shen, H., Yang, D., He, Y., 2017. Using Landsat 8 data to estimate suspended particulate matter in the Yellow River estuary. *J. Geophys. Res.* 122, 276–290.
- Rodgers, K.U.S., Jokiel, P.L., Brown, E.K., Hau, S., Sparks, R., 2015. Over a decade of change in spatial and temporal dynamics of Hawaiian coral reef communities. *Pac. Sci.* 69, 1–13.
- Roy, D.P., Wulder, M.A., Loveland, T.R., Woodcock, C.E., Allen, R.G., Anderson, M.C., Helder, D., Irons, J.R., Johnson, D.M., Kennedy, R., Scambos, T.A., Schaaf, C.B., Schott, J.R., Sheng, Y., Vermote, E.F., Belward, A.S., Bindschadler, R., Cohen, W.B., Gao, F., Hippel, J.D., Hostert, P., Huntington, J., Justice, C.O., Kilic, A., Kovalevskyy, V., Lee, Z.P., Lymburner, L., Masek, J.G., McCorkel, J., Shuai, Y., Trezza, R., Vogelmann, J., Wynne, R.H., Zhu, Z., 2014. Landsat-8: science and product vision for terrestrial global change research. *Remote Sens. Environ.* 145, 154–172.
- Salama, M.S., Melin, F., Van der Velde, R., 2011. Ensemble uncertainty of inherent optical properties. *Opt. Express* 19, 16772–16783.
- Santer, R., Schmechtig, C., 2000. Adjacency effects on water surfaces: primary scattering approximation and sensitivity study. *Appl. Opt.* 39, 361–375.
- Schott, J.R., Gerace, A., Woodcock, C.E., Wang, S., Zhu, Z., Wynne, R.H., Blinn, C.E., 2016. The impact of improved signal-to-noise ratios on algorithm performance: case studies for Landsat class instruments. *Remote Sens. Environ.* 185, 37–45.
- Shang, Z., Lee, Z., Dong, Q., Wei, J., 2017. Self-shading associated with a skylight-blocked approach system for the measurement of water-leaving radiance and its correction. *Appl. Opt.* 56, 7033–7040.
- Stumpf, R.P., Holderied, K., Sinclair, M., 2003. Determination of water depth with high-resolution satellite imagery over variable bottom types. *Limnol. Oceanogr.* 48, 547–556.
- Taylor, D.I., 2016. Boston Harbor Water Quality (1994–2015). Massachusetts Water Resources Authority, Boston, MA, pp. 14.
- Turner, W., Rondinini, C., Pettorelli, N., Mora, B., Leidner, A.K., Szantoi, Z., Buchanan, G., Dech, S., Dwyer, J., Herold, M., Koh, L.P., Leimgruber, P., Taubenboeck, H., Wegmann, M., Wikelski, M., Woodcock, C., 2015. Free and open-access satellite data are key to biodiversity conservation. *Biol. Conserv.* 182, 173–176.
- Vanhellemont, Q., Ruddick, K., 2014. Turbid wakes associated with offshore wind turbines observed with Landsat 8. *Remote Sens. Environ.* 145, 105–115.
- Vanhellemont, Q., Ruddick, K., 2015. Advantages of high quality SWIR bands for ocean colour processing: examples from Landsat-8. *Remote Sens. Environ.* 161, 89–106.
- Vermote, E., Justice, C., Claverie, M., Franch, B., 2016. Preliminary analysis of the performance of the Landsat 8/OLI land surface reflectance product. *Remote Sensing of Environment* 185, 46–56.
- Voss, K.J., McLean, S., Lewis, M., Johnson, C., Flora, S., Feinholz, M., Yarbrough, M., Trees, C., Twardowski, M.S., Clark, D., 2010. An example crossover experiment for testing new vicarious calibration techniques for satellite ocean color radiometry. *J. Atmos. Ocean. Technol.* 27, 1747–1759.
- Wang, M., Bailey, S., 2001. Correction of the sun glint contamination on the SeaWiFS ocean and atmosphere products. *Appl. Opt.* 40, 4790–4798.
- Wang, M., Shi, W., 2007. The NIR-SWIR combined atmospheric correction approach for MODIS ocean color data processing. *Opt. Express* 15, 15722–15733.
- Wedding, L.M., Lecky, J., Gove, J.M., Walecka, H.R., Donovan, M.K., Williams, G.J., Jouffray, J.-B., Crowder, L.B., Erickson, A., Falinski, K., Friedlander, A.M., Kappel, C.V., Kittinger, J.N., McCoy, K., Norström, A., Nyström, M., Oleson, K.L.L., Stamoulis, K.A., White, C., Selkoe, K.A., 2018. Advancing the integration of spatial data to map human and natural drivers on coral reefs. *PLoS One* 13, e0189792.
- Wei, J., Lee, Z.P., 2015. Retrieval of phytoplankton and color detrital matter absorption coefficients with remote sensing reflectance in an ultraviolet band. *Appl. Opt.* 54, 636–649.
- Wei, J., Lee, Z.P., Lewis, M., Pahlevan, N., Ondrusek, M., Armstrong, R., 2015. Radiance transmittance measured at the ocean surface. *Opt. Express* 23, 11826–11837.
- Wei, J., Lee, Z.P., Shang, S., 2016. A system to measure the data quality of spectral remote sensing reflectance of aquatic environments. *J. Geophys. Res.* 121, 8189–8207.
- Yadav, S., Yoneda, M., Susaki, J., Tamura, M., Ishikawa, K., Yamashiki, Y., 2017. A satellite-based assessment of the distribution and biomass of submerged aquatic vegetation in the optically shallow basin of Lake Biwa. *Remote Sens.* 9, 966.
- Zhang, M., Hu, C., Kowalewski, M.G., Janz, S.J., Lee, Z.P., Wei, J., 2017. Atmospheric correction of hyperspectral airborne GCAS measurements over the Louisiana Shelf using a cloud shadow approach. *Int. J. Remote Sens.* 38, 1162–1179.
- Zheng, Z., Ren, J., Li, Y., Huang, C., Liu, G., Du, C., Lyu, H., 2016. Remote sensing of diffuse attenuation coefficient patterns from Landsat 8 OLI imagery of turbid inland waters: a case study of Dongting Lake. *Sci. Total Environ.* 573, 39–54.
- Zibordi, G., Holben, B., Hooker, S.B., Mélin, F., Berthon, J.F., Slutsker, I., Giles, D., Vandemark, D., Feng, H., Rutledge, K., Schuster, G., Mandoos, A.A., 2006. A network for standardized ocean color validation measurements. *EOS Trans. Am. Geophys. Union* 87, 293–297.
- Zibordi, G., Berthon, J.-F., Mélin, F., D'Alimonte, D., Kaitala, S., 2009a. Validation of satellite ocean color primary products at optically complex coastal sites: Northern Adriatic Sea, Northern Baltic Proper and Gulf of Finland. *Remote Sens. Environ.* 113, 2574–2591.
- Zibordi, G., Holben, B.N., Slutsker, I., Giles, D., D'Alimonte, D., Melin, F., Berthon, J.-F., Vandemark, D., Feng, H., Schuster, G., Fabbri, B.E., Kaitala, S., Seppala, J., 2009b. AERONET-OC: a network for the validation of ocean color primary products. *J. Atmos. Ocean. Technol.* 26, 1634–1651.